MATERIALS CHEMISTRY FRONTIERS

RESEARCH ARTICLE

View Article Online
View Journal | View Issue

Cite this: *Mater. Chem. Front.*, 2023, **7**, 3127

Engineering raspberry-like $CuCo_2S_4$@ZnS hollow particles encapsulated with reduced graphene oxide for hybrid supercapacitors†

Bahareh Ameri, Akbar Mohammadi Zardkhoshoui* and Saied Saeed Hosseiny Davarani *

Transition-metal sulfides (TMSs) stand out as promising materials for supercapacitors due to their plentiful electroactive sites and relatively high conductivity compared with their oxide counterparts. Among them, copper–cobalt sulfides are regarded as effective active materials, but their specific capacity and cycling durability cannot meet expectations. To mitigate these issues, elaborate synthesis and design of hollow nanostructures with high complexity have been considered an effective approach. Also, hybridizing reduced graphene oxide (rGO) with complex hollow nanostructures to improve capacity behaviors, enhance electrical conductivity, and enlarge the surface area is highly desired. Considering this, in this work, we demonstrate the construction of raspberry-like $CuCo_2S_4$@ZnS hollow particles (RCCS-ZSH), in which the $CuCo_2S_4$ hollow nanospheres (CCS-HSs) are well confined in the porous ZnS shells. By controlling the sulfidation reaction time during the sulfidation reactions, an optimized sample (RCCS-ZSH8) was achieved with superior electrochemical performance. Then, the as-prepared RCCS-ZSH8 nanostructures were encapsulated in the rGO network (RCCS-ZSH8-rGO) to form a unique nanoarchitecture. In such a structure, the RCCS-ZSH8 nanostructures are characterized by abundant electroactive sites and easy ion diffusion. More importantly, the encapsulating of the rGO network around RCCS-ZSH8 particles not only endows the composites with better electrical conductivity but also inhibits the aggregation of particles and maintains structural durability throughout the longevity test. Therefore, the RCCS-ZSH8-rGO-based electrode presents tremendous supercapacitive properties with its attractive capacity of 1346 C g^{-1} and excellent longevity (95.4%) after 10 000 cycles. Eventually, a hybrid supercapacitor apparatus (RCCS-ZSH8-rGO//AC) based on the RCCS-ZSH8-rGO cathode and activated carbon (AC) anode exhibits a reasonable energy/power density of 64.2 W h kg^{-1}/802.5 W kg^{-1} and remarkable durability (92.8% of initial capacity for 10 000 cycles at 8 A g^{-1}). This research thus presents a useful protocol for the rational engineering of rGO-encapsulated complex hollow nanostructures for various applications.

Received 27th February 2023,
Accepted 18th April 2023

DOI: 10.1039/d3qm00212h

rsc.li/frontiers-materials

Introduction

Owing to the environmental pollution consequences resulting from the ever-amplifying population and depletion of fossil fuels, the rapid evolution of energy storage devices (ESDs) including fuel cells, supercapacitors, and batteries has garnered considerable attention.[1,2] As of now, supercapacitors and batteries are extensively used to store energy.[3–5] In contrast to batteries, supercapacitors have great potential for various applications owing to their several advantages including longer operating time, fast charge/discharge potency, optimal power density, and environmental sustainability.[6–14] Despite these encouraging properties, low energy density (ED) delivered by supercapacitors is a bottleneck impeding their utilization in practical applications.[15–17]

As a kind of favorable ESD, hybrid supercapacitors, which are composed of battery-type materials and capacitor-type anode materials, have become research hotspots as they can produce desired energy density and power density. Due to the combination of a battery-like material to supply a high energy density and a capacitive electrode to supply a desirable power density, hybrid supercapacitors show widened cell voltage and enhanced energy density without

Department of Chemistry, Shahid Beheshti University, G. C., 1983963113, Evin, Tehran, Iran. E-mail: mohammadi.bahadoran@gmail.com, ss-hosseiny@sbu.ac.ir; Fax: +98 21 22431661; Tel: +98 21 22431661

† Electronic supplementary information (ESI) available: supplementary characterization and electrochemical data, and a benchmark table to compare the performance of the as-prepared device with previous reports are presented. See DOI: https://doi.org/10.1039/d3qm00212h

sacrificing high power density in comparison with traditional supercapacitors.[18–23]

The electrochemical characteristics of hybrid supercapacitors are mostly controlled by their battery-like materials, and hence selecting appropriate active materials is crucial for hybrid supercapacitors. Among many battery-like materials, cobalt-based materials are extensively used in hybrid supercapacitors due to their reasonable electrical conductivity, high natural abundance, and high specific capacity. On the other side, the better conductivity of copper (5.96×10^7 S m^{-1}) than that of other metals such as nickel (1.43×10^7 S m^{-1}) and manganese (2.07×10^6 S m^{-1}) offers a favorable candidate of copper cobalt sulfide for hybrid supercapacitors.[18–20]

TMSs have drawn particular attention as hopeful active materials for hybrid supercapacitors, thanks to their good thermal stability, high conductivity, and low cost.[24–26] In comparison to monometallic sulfides, bimetallic sulfides show better conductivity and richer redox reactions.[27,28] Especially, $CuCo_2S_4$ (CCS) with its merits of environmental compatibility, natural abundance, and good theoretical capacity has stimulated huge research interest.[29–31] For instance, You *et al.* reported the synthesis of hollow CCS spheres *via* a solvothermal route, which manifested a capacitance of 1137.5 F g^{-1} with a rate performance of 84.8%.[32] In another approach, Jia *et al.* prepared urchin-like CCS microspheres *via* a hydrothermal process, which exhibited a capacitance of 1069 F g^{-1} with a rate performance of 61.2%.[33] Similarly, Han *et al.* prepared CCS nanobelt arrays that showed a good capacity of 1014 C g^{-1} with a notable longevity of 93.82%.[34]

The intrinsic properties of the CCS such as sluggish reaction kinetics, low electrical conductivity, and inadequate numbers of electroactive sites, which arise from its inherently poor charge transfer capability and limited low-valence metallic cation containment, have become principal drawbacks for its applications.[35] These drawbacks could be addressed using different approaches including, but not limited to (1) surface coating electrode material with appropriate active materials to enhance the redox reaction and improve the electrical conductivity,[10] (2) fabrication and structural design of electrode materials that could provide higher electroactive sites,[36,37] and (3) designing complex hollow nanoarchitectures encapsulated within conductive carbonaceous materials.[8,36,37]

Zinc sulfide (ZnS) has been considered an appropriate active material due to its promising electrochemical properties, low cost, easy fabrication, good electrical conductivity, nontoxicity, environmental friendliness, and a wide band gap of 3.5 to 3.8 eV.[38,39] In recent years, there have been several studies reported on the introduction of ZnS into electrode materials to produce suitable active materials. For instance, Ikkurthi *et al.* synthesized NiS/ZnS by a chemical bath deposition route that could be used as a cathode in supercapacitors providing a capacitance of 1533 F g^{-1}, which was higher than that of NiS alone.[38] Further improvement was achieved by Chen *et al.*, who used a metal–organic framework-assisted method to fabricate a Co_9S_8@Ni_3S_2/ZnS composite with an areal capacity of 8192 C cm^{-2} at 2 mA cm^{-2}.[40] Considering the intrinsic potential of ZnS, incorporating a well-designed structure may improve the durability and performance of electrodes designed using ZnS.

In addition to electrode composition, the structural features could impact the supercapacitive features.[41–43] For instance, the use of hollow structures could provide a high surface area, excellent permeability, rich electroactive sites, and shortened distance for charge transportation.[44,45] To date, hollow structures have been widely used in diverse fields such as drug delivery, batteries, catalysis, supercapacitors, and solar cells.[44,45] Nowadays, much effort has been devoted to optimizing the structural properties of hollow structures aimed at obtaining improved mass diffusion properties and increased surface areas.[44,45] Among various hollow structures, complex hollow architectures with multi-shells or multi-cavities/channels have shown better electrochemical performance compared to simple hollow counterparts.[46,47] This could be due to the higher content of electroactive species within the hollow particles.[48] However, the controllable synthesis of hollow nanostructures remains a serious challenge.

Metal–organic frameworks (MOFs) composed of a broad range of organic ligands and metal species have been widely explored as sacrificial templates for the synthesis of various hollow materials owing to their simple fabrication, porous structure, and ease of tunability.[49,50] The ZIFs are the subclass of MOFs and have received great interest.[51,52] Previous studies revealed that ZIF-8 made of zinc metal nodes and a 2-methylimidazole linker can be utilized as a sacrificial template to fabricate zinc-based oxides and sulfides.[53,54]

In addition to the reasonable design of complex hollow nanoarchitectures, combining suitable carbonaceous materials is another useful approach to achieve materials with enhanced supercapacitive performance. Among carbon materials, graphene with good conductivity, robust structural stability, and large surface area is a favorable candidate.[36,37] Previous studies have proven that the graphene network acts as the protective skeleton to enhance the structural durability of TMSs and inhibit the aggregation of particles, resulting in excellent longevity.[8,36,37]

Considering these, in this study, we designed a new cathode material consisting of encapsulated raspberry-like $CuCo_2S_4$@ZnS hollow spheres in a rGO network (RCCS-ZSH-rGO) that was explored as an electrode for hybrid supercapacitors. A hybrid supercapacitor was then fabricated using RCCS-ZSH-rGO, and it delivered a high energy density and durability. Our further assessments suggested that besides the intrinsic properties of rGO and $CuCo_2S_4$@ZnS, the high performance of the designed device is mainly attributed to the structural advantages of RCCS-ZSH-rGO which can be summed up as follows: (1) the RCCS-ZSH particles enable rich electroactive sites; (2) the encapsulating rGO skeleton forms an effective layer, enhancing the conductivity of the material; and (3) the rGO skeleton can serve as a layer, inhibiting the aggregation of RCCS-ZSH particles and preserving the structural integrity.

Experimental section

Chemicals

Herein, the chemicals used were C_3H_8O [isopropanol], $Cu(NO_3)_2{\cdot}6H_2O$ [copper(II) nitrate hexahydrate], $C_3H_8O_3$ [glycerol], $Co(NO_3)_2{\cdot}6H_2O$ [cobalt(II) nitrate hexahydrate], C_2H_5OH [ethanol], $C_4H_6N_2$ [2-methylimidazole], $Zn(NO_3)_2{\cdot}6H_2O$ [zinc nitrate hexahydrate], CH_3OH [methanol], and C_2H_5NS [thioacetamide].

Generation of CC-G spheres

The CC-G spheres were prepared through a hydrothermal route. Typically, $Cu(NO_3)_2{\cdot}6H_2O$ (36.95 mg) and $Co(NO_3)_2{\cdot}6H_2O$ (72.75 mg) were fully dissolved in a mixed solution of C_3H_8O (40 mL) and $C_3H_8O_3$ (8 mL) with vigorous stirring to produce a homogeneous solution. The resulting mixture was poured into a clean autoclave and heated at 180 °C for 6 h. Then, the CC-G sample was produced through centrifugation, rinsed with H_2O and C_2H_5OH repeatedly, and then dried at 70 °C for 15 h.

Generation of CC-G@ZIF-8

4 mg of the as-prepared CC-G powder was dissolved in 20 mL of 20 mM $Zn(NO_3)_2{\cdot}6H_2O$ methanol solution for 20 min. Then, 20 mL of 20 mM $C_4H_6N_2$ methanol solution was added. After reaction for 24 h, the sample was carefully collected and then rinsed with C_2H_5OH 6 times.

Generation of RCCS-ZSH particles

The CCG@ZIF-8 was transferred into a C_2H_5OH (10 mL) solution containing 20 mg of C_2H_5NS. The sulfidation process was conducted at 140 °C for 8 h. The RCCS-ZSH particles were collected using centrifugation and rinsed with C_2H_5OH 6 times and denoted as RCCS-ZSH8. For comparison, three samples were also fabricated with sulfidation times of 4, 6, and 10 h at 140 °C, denoted as RCCS-ZSH4, RCCS-ZSH6, and RCCS-ZSH10, respectively. In addition, CCS-HSs without ZnS were prepared *via* a similar process. Similarly, porous ZnS nanocages without CCS-HSs were obtained.

Generation of RCCS-ZSH8-rGO

Graphene oxide was prepared by using Hummers' route.[8] The RCCS-ZSH8-rGO sample was synthesized through direct annealing of the RCCS-ZSH8 composite that was mixed with the GO layer. Typically, 100 mg of the RCCS-ZSH8 powder was first dispersed in 100 mL of H_2O and ultrasonically treated for 1 h. Then, 20 mL of a homogeneous GO (8 mg mL^{-1}) aqueous suspension was carefully added into the RCCS-ZSH8 suspension under magnetic stirring for 5 h. Finally, the mixed suspension was collected *via* centrifugation and then treated at 500 °C for 4 h in an Ar atmosphere to achieve the reduction of GO. For comparison, two concentrations of GO suspension (6 mg mL^{-1} and 10 mg mL^{-1}) were also used. Note that, the samples were labeled RCCS-ZSH8-rGO-*x*, where *x* = 1, 2, and 3 means that the concentrations of GO suspension are 6 mg mL^{-1}, 8 mg mL^{-1}, and 10 mg mL^{-1}, respectively.

Characterization techniques

The crystallinity description of the resulting samples was recognized using X-ray diffraction [XRD; Philips X'Pert Pro X-ray diffractometer]. The surface morphological investigations were probed *via* field-emission scanning electron microscopy [FE-SEM; MIRA 3 TESCAN; 15 kV, Czech], combined with energy-dispersive X-ray (EDX) spectroscopy. The interior structure of the resulting samples was investigated through transmission electron microscopy [TEM; Philips CM200 instrument]. The element valence of the optimized RCCS-ZSH8-rGO2 was detected by X-ray photoelectron spectrometry [XPS; Thermo Scientific: ESCALAB 250Xi Mg X-ray source]. The specific surface area (SSA) and pore-size distribution (PSD) of the RCCS-ZSH8-rGO2, RCCS-ZSH8, CCSHS, and ZS were analyzed using the Brunauer–Emmett–Teller (BET) method and Barrett–Joyner–Halenda (BJH) analysis, respectively.

Electrochemical studies

Three-electrode setup

An Autolab PGSTAT 204 system (Echo Chemie; Netherlands) was employed to check the supercapacitive features of all materials. Basic measurements like EIS, GCD, and CV were conducted on a three-electrode setup to explore the performance of all electrodes. This setup was made of the fabricated electrode materials, Ag/AgCl, and platinum (Pt) wire, which served as the working, reference, and counter electrodes, respectively, and all tests were performed in 6 M KOH. Note that, nickel foam was used as a suitable current collector in this work, thanks to its good conductivity and multi-dimensional skeleton to support the as-fabricated active materials.[26] The slurry coating route was employed to generate the working electrodes. Before coating the as-fabricated active materials on the current collector, the NF was thoroughly cleaned.[26] The cleaning procedure was carried out as follows: first ultrasonication in HCl (3.0 M) and then ultrasonication was continued with H_2O, C_3H_6O, and C_2H_5OH. Finally, the nickel foam was fully dried for 24 h. The working electrodes were fabricated by grinding the synthesized samples (80 wt%), carbon black (10 wt%), and polyvinylidene fluoride (10 wt%) in a mortar using an appropriate *N*-methyl 2-pyrrolidone solvent. Thereafter, the slurry was painted on the nickel foam (NF, 1 × 1 cm^2 active area) with a brush and dried at 70 °C in an oven for 8 h. Afterward, the electrode was pressed up to 10 MPa to the strong attachment of active material with the NF. The mass loading of all samples on NF was calculated to be 4.0 mg. The specific capacity (C_s: C g^{-1}) values of the as-made electrodes were obtained from the GCD plots using eqn (1):[55]

$$C_s(\mathrm{C\ g^{-1}}) = \frac{2I \times \int V\,\mathrm{d}t}{m \times V} \quad (1)$$

where C_s represents the capacity of electrodes (C g^{-1}), m stands for mass loading of samples (g), I displays discharge current (A), V reflects voltage window (V), and dt reveals the discharge time (s). Also, the Coulombic efficiency (η) of the RCCS-ZSH8-rGO2-based

electrode and hybrid device was calculated from eqn (2):[6,10,12]

$$\eta = \frac{t_d}{t_c} \quad (2)$$

where t_d (s) and t_c (s) signify the discharging and charging time, respectively.

Designing of RCCS-ZSH8-rGO2//AC

The RCCS-ZSH8-rGO2//AC hybrid supercapacitor was designed by using the RCCS-ZSH8-rGO2 material as a propitious cathode and AC as an anode with 6 M KOH. Also, the anode electrode was a crucial element in the fabrication of RCCS-ZSH8-rGO2// AC. Here, AC was preferred as an appropriate anode due to its satisfactory electrochemical conductivity, high porosity, and robust mechanical stability.[26] The anode electrode was also fabricated by a similar method as referred to in the foregoing section.

Before the fabrication of RCCS-ZSH8-rGO2//AC, both anode (AC) and cathode (RCCS-ZSH8-rGO2) electrodes were dipped in KOH to achieve excellent electrochemical outcomes in a two-electrode setup. A piece of cellulose paper with suitable dimensions was carefully inserted in between the RCCS-ZSH8-rGO2 and AC electrodes and then they were assembled. The full arrangement was carefully inserted into a pouch-like bag and then sealed after injecting a few mL of KOH. The cellulose paper prevents the short circuit and accelerates the mobility of the KOH electrolyte in between them.[26] According to the calculation from eqn (3), the mass ratio of RCCS-ZSH8-rGO2 and AC electrodes was fixed at 1 : 7.2 to attain the best performance of RCCS-ZSH8-rGO2//AC by charge balancing:[55]

$$\frac{m_+}{m_-} = \frac{C_- \times \Delta V_-}{C_{s+}} \quad (3)$$

In eqn (3), ΔV refers to the voltage window, C specifies the capacitance (F g^{-1}), and m_- indicates the mass for the AC, respectively. Besides, m_+ refers to the mass for the RCCS-ZSH8-rGO2 and C_{s+} exhibits the capacity (C g^{-1}) for RCCS-ZSH8-rGO2. The mass loading for fabricating RCCS-ZSH8-rGO2//AC was ~4.0 and ~29 mg for RCCS-ZSH8-rGO2 and AC electrodes, respectively. The energy (E; W h kg^{-1}) and power density (P; W kg^{-1}) of the RCCS-ZSH8-rGO2//AC were evaluated from the following formulas:[55]

$$E(\mathrm{W\,h\,kg^{-1}}) = \frac{I\int V\,dt}{3.6 \times M} \quad (4)$$

$$P(\mathrm{W\,kg^{-1}}) = \frac{E}{\Delta t} \times 3600 \quad (5)$$

In eqn (4), M specifies the total mass of materials on both the anode and cathode and Δt is the discharging time.

Results and discussion

The synthesis process of RCCS-ZSH8-rGO2 is schematically depicted in Fig. 1. We first developed a solvothermal strategy to prepare CC-G spheres as the precursors. Then, ZIF-8 was grown onto the CC-G spheres at room temperature, forming the core–shell CC-G@ZIF-8 structures. Subsequently, the CC-G@ZIF-8 was converted into RCCS-ZSH8 after the sulfidation reaction. Finally, the RCCS-ZSH8 nanostructures were encapsulated with the rGO network to form RCCS-ZSH8-rGO2.

The morphological features of the products were scrutinized by FE-SEM and TEM. The FE-SEM and TEM images of the CC-G verify the rigid nature of the product with a very smooth surface (Fig. S1(a–c), ESI†). The EDX pattern of CC-G demonstrates that our product is composed of Cu, Co, O, and C elements (Fig. S1(d), ESI†).

The CC-G spheres were converted into CCS-HSs after the sulfidation reaction *via* TAA and the morphologies of the as-synthesized CCS-HSs are presented in Fig. S2 (ESI†). A sulfidation process was used to convert the CuCo–glycerate (CC-G) solid spheres into the $CuCo_2S_4$ hollow spheres. After sulfidation for 4 h, the S^{2-} ions obtained from the decomposition of C_2H_5NS reacted with Cu^{2+} and Co^{2+} on the surface of CuCo–glycerate and produced CuCo–glycerate@$CuCo_2S_4$ core–shell nanostructures.[43] During sulfidation for 6 h, inward diffused S^{2-} ions and outward-diffused Cu^{2+} and Co^{2+} ions facilitated the growth of the $CuCo_2S_4$ shell, resulting in a distinct gap between the shell and the CuCo–glycerate yolk. At the end of the reaction, with the progress of sulfidation for 8 h, the inner CuCo–glycerate solid sphere became diminished, and unique $CuCo_2S_4$ hollow spheres were obtained owing to the discrepancy in the diffusion rate between Cu^{2+} and Co^{2+} cations and S^{2-} anions.[43] As reflected in Fig. S2(a) (ESI†), the CCS-HSs obtained were very uniform and inherited the spherical-like shape of CC-G. From the increased surface roughness revealed in the magnified images (Fig. S2(b and c), ESI†), it can be concluded that these CC-G spheres were transformed into CCS-HSs. The EDX pattern of CCS-HS manifests the presence of S, Cu, and Co with atomic percentages of 57.23%, 14.25%, and 28.52%, respectively, confirming the successful fabrication

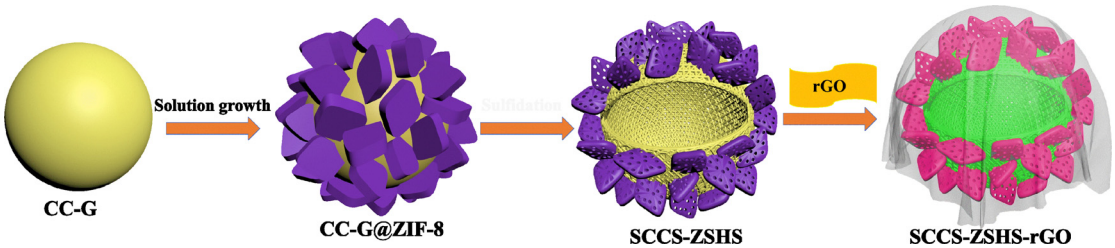

Fig. 1 Schematic diagram for the synthesis of the RCCS-ZSH8-rGO2 sample.

of CCS-HSs (Fig. S3, ESI†). As shown in the corresponding FE-SEM mapping results (Fig. S4, ESI†), the CCS-HSs consist of Cu, Co, and S elements. As further demonstrated by TEM observation (Fig. S5, ESI†), hollow/porous spheres can be observed for the CCS-HS sample.

The FE-SEM image of pure ZIF-8 demonstrates that the pure ZIF-8 particles are highly uniform (Fig. S6(a), ESI†). As reflected in Fig. S6(b) (ESI†), it was found that the ZIF-8 particles have a rhombic dodecahedral shape with a smooth surface. The as-obtained ZIF-8 was then converted to ZnS through a sulfidation reaction. During the sulfidation reaction, the sulfide ions from the decomposition of TAA reacted with the Zn ions on the surface of ZIF-8 and generated ZnS nanostructures.[56] A low-magnification FE-SEM image (Fig. S7(a), ESI†) reflects that the ZnS nanocages were uniform. A magnified FE-SEM image represents the polyhedral shape of ZnS particles with rough surfaces (Fig. S7(b), ESI†). The EDX pattern of ZnS reflects the presence of Zn and S with atomic percentages of 49.81% and 50.19%, respectively, which validates the fabrication of ZnS nanocages (Fig. S8, ESI†). As revealed from FE-SEM mapping images, Zn and S elements were distributed throughout the ZnS (Fig. S9, ESI†). More morphological information was obtained by TEM. Fig. S10 (ESI†) reflects the TEM image of ZnS. It can be seen that ZnS derived from ZIF-8 possesses a porous nature.

To study the structural evolution process from CC-G to RCCS-ZSH8, the intermediate products were obtained at several reaction times. To gain better understanding of the formation process of the RCCS-ZSH8 sample, investigations using FE-SEM and TEM were carried out. The FE-SEM image discloses that CC-G@ZIF-8 particles inherited the spherical shape of the CC-G (Fig. 2(a)). The magnified image (Fig. 2(b)) of one single CC-G@ZIF-8 particle demonstrates that the surface of the spheres was composed of ZIF-8 particles. Besides, the EDX pattern of CC-G@ZIF-8 indicates that the product was made up of Cu, Co, C, N, Zn, and O elements (Fig. S11, ESI†). After sulfidation of CC-G@ZIF-8 for 4 h in the presence of C_2H_5NS, the product reflected a rougher surface (Fig. 2(c and d)), demonstrating the occurrence of the sulfidation reaction on the surface, and raspberry-like particles were obtained. Fig. 2(e) and (f) represent the FE-SEM images of CC-G@ZIF-8 after sulfidation for 6 h. The obtained FE-SEM images demonstrate that the sample inherited a raspberry-like morphology with a rough surface. After sulfidation for 8 h, the sulfidation reaction was ended and the surface of the product showed significant roughness (Fig. 2(g and h)). As evidenced from the image of the optimized RCCS-ZSH8 sample, the raspberry-like morphology was well preserved even after the sulfidation for 8 h (Fig. 2(h)). When the sulfidation time was extended to 10 h, as shown in Fig. 2(i and j), the particles were extensively damaged and the surface roughness features of the particles became more pronounced. At the same time, the structure of the particles collapsed, which was mainly due to the over-sulfidation of the particles.[34] As shown in Fig. S12 (ESI†), the EDX spectrum of RCCS-ZSH8 manifested the elemental peaks of Cu, Co, Zn, and S with atomic percentages of 11.05%, 22.12%, 11.03%, and 55.8%, respectively, which corroborates the successful synthesis of the

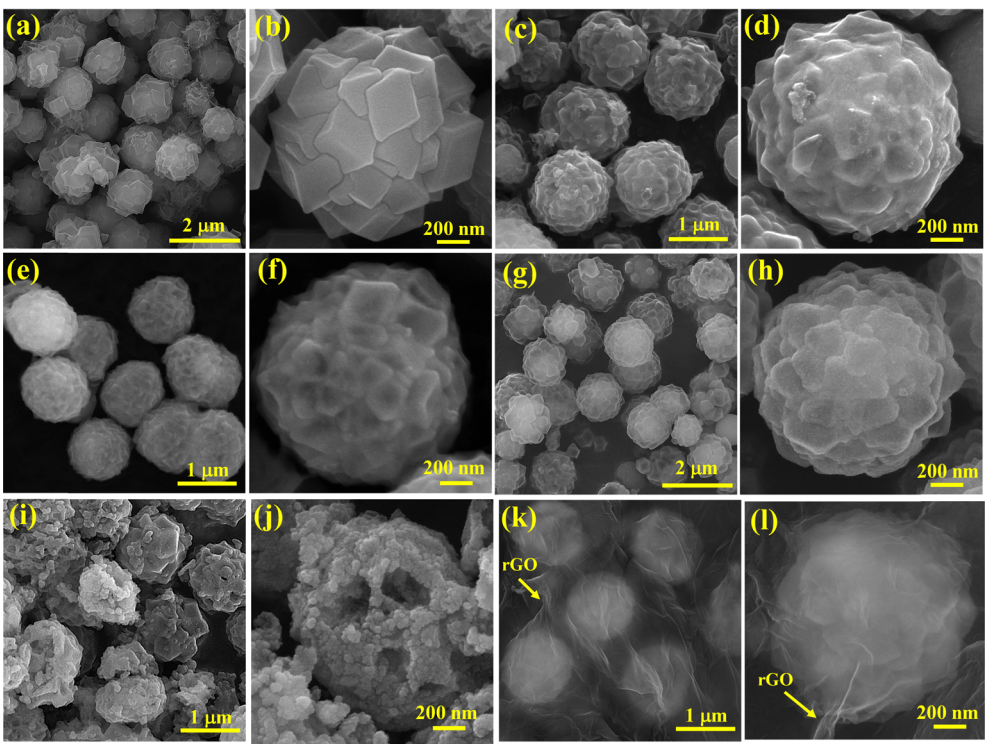

Fig. 2 (a and b) FE-SEM images of the CC-G@ZIF-8 sample. (c and d) FE-SEM images of the CC-G@ZIF-8 sample after sulfidation for 4 h. (e and f) FE-SEM images of the CC-G@ZIF-8 sample after sulfidation for 6 h. (g and h) FE-SEM images of the CC-G@ZIF-8 sample after sulfidation for 8 h. (l and j) FE-SEM images of the CC-G@ZIF-8 sample after sulfidation for 10 h. (k and l) FE-SEM images of the RCCS-ZSH8-rGO2 sample.

RCCS-ZSH8. As revealed in Fig. S13 (ESI†), the corresponding FE-SEM mappings further verify the homogeneous distribution of Cu, Co, Zn, and S in RCCS-ZSH8.

Fig. 2(k, l) and Fig. S14 (ESI†) manifest the morphological changes in RCCS-ZSH8-rGO nanocomposites with 6, 8, and 10 mg mL^{-1} GO. As reflected in Fig. 2(k), when the concentration of GO was 8 mg mL^{-1}, the RCCS-ZSH8 nanostructures were well-wrapped with the rGO layer (indicated by arrows), and particles separated from each other, creating a 3D network. A magnified FE-SEM image of RCCS-ZSH8-rGO2 clearly demonstrates that RCCS-ZSH8-rGO2 inherits the spherical shape of RCCS-ZSH8, while the RCCS-ZSH8 nanostructures are well-encapsulated within the rGO network (Fig. 2(l)). In addition, when the concentration of GO was 6 mg mL^{-1} (RCCS-ZSH8-rGO1), it can be evidently observed that the particles still aggregated with each other (Fig. S14(a), ESI†). As illustrated in Fig. S14(b) (ESI†), when the concentration of GO was 10 mg mL^{-1} (RCCS-ZSH8-rGO3), the RCCS-ZSH8 particles were well separated, but the particles were encapsulated in a large amount of rGO, which reduced the performance of the whole electrode (demonstrated in the discussion on supercapacitive performance). The EDX analysis of RCCS-ZSH8-rGO2 (Fig. S15, ESI†) revealed that the weight percentage of Cu, Co, Zn, S, C, and O elements in RCCS-ZSH8-rGO2 was about 6.86%, 14.12%, 6.55%, 44.45%, 20.15%, and 7.87%. Accordingly, the contents of $CuCo_2S_4$, ZnS, and rGO in RCCS-ZSH8-rGO2 are estimated to be 56.54 wt%, 15.44 wt%, and 28.02 wt%, respectively. Hence, the weight ratio of $CuCo_2S_4$, ZnS, and rGO in RCCS-ZSH-rGO2 can be calculated to be approximately 1.83 : 0.50 : 0.90. Besides, the elemental mappings of RCCS-ZSH8-rGO2 reveal that Cu, Co, S, Zn, and C were dispersed in RCCS-ZSH8-rGO2, as manifested in Fig. S16 (ESI†). These results demonstrate the successful preparation of the RCCS-ZSH8-rGO2 sample.

The intrinsic morphological properties of the as-prepared products were also investigated using TEM. Fig. 3 shows the TEM images of metal sulfide products formed at several sulfidation times and the RCCS-ZSH8-rGO2 sample. It can be seen that ZIF-8 particles were grown on CC-G solid spheres at room temperature, and the thickness of the ZIF-8 layer was 200 nm (Fig. 3(a1 and a2)). As reflected in Fig. 3(a1 and a2), the TEM images of the as-made sample display a clear core–shell morphology with the outer shell (ZIF-8) having a lighter contrast. After sulfidation of the precursor for 4 h, the resulting yolk–sell structure contained two shells, with the outer shell corresponding to ZIF-8 (Fig. 3(b1 and b2)). When the reaction time was extended to 6 h, the porosity of both shells increased (Fig. 3(c1 and c2)). When the sulfidation time was prolonged to 8 h, the inner spheres with solid nature were transformed into hollow structured nanospheres, forming RCCS-ZSH-8 nanostructures (Fig. 3(d1 and d2)). These results demonstrate the successful conversion of CC-G@ZIF-8 into RCCS-ZSH8 particles through the sulfidation reaction.

As expected, the RCCS-ZSH8 particles which were encapsulated in the rGO network can also be easily identified in the TEM images (Fig. 3(e1 and e2)), and the folded rGO nanosheets (indicated by arrows) are observed around RCCS-ZSH8. Due to the flexible and extremely thin nature of the rGO skeleton, the SCCS-ZSH8 particles could be observed, suggesting a good interfacial contact between SCCS-ZSH8 particles and rGO (indicated by arrows). The formation process of RCCS-ZSH8-rGO2 is also schematically shown in Fig. 3(a3–e3). The existing rGO skeleton around RCCS-ZSH8 not only served as an excellent conductive film to boost the conductivity of the sample but also

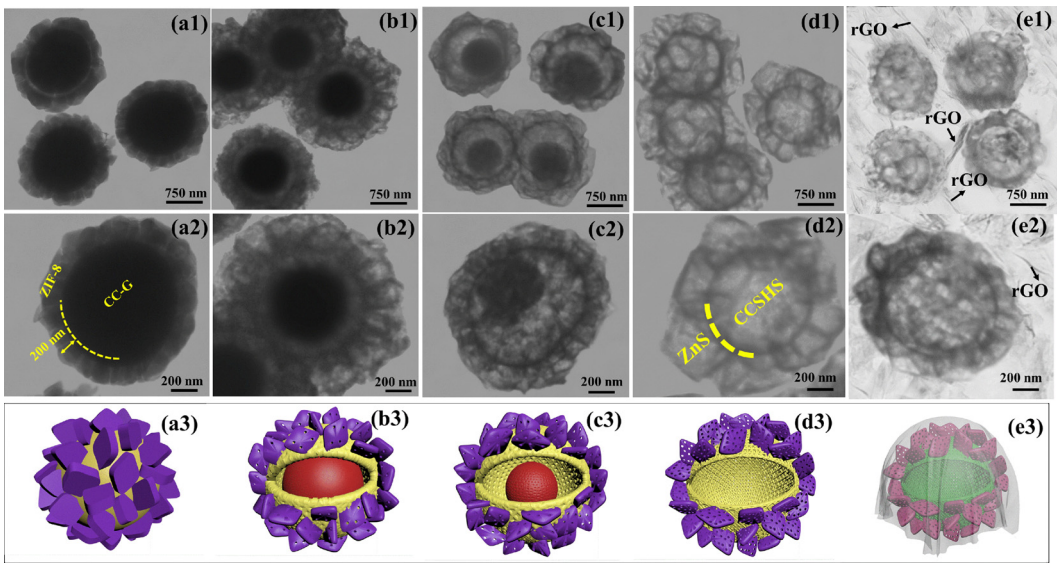

Fig. 3 (a1–a3) TEM images and the corresponding schematic illustration of CC-G@ZIF-8. (b1–b3) TEM images and the corresponding schematic illustration of CC-G@ZIF-8 after sulfidation for 4 h. (c1–c3) TEM images and the corresponding schematic illustration of CC-G@ZIF-8 after sulfidation for 6 h. (d1–d3) TEM images and the corresponding schematic illustration of the RCCS-ZSH8 sample. (e1–e3) TEM images and the corresponding schematic illustration of the RCCS-ZSH8-rGO2 sample.

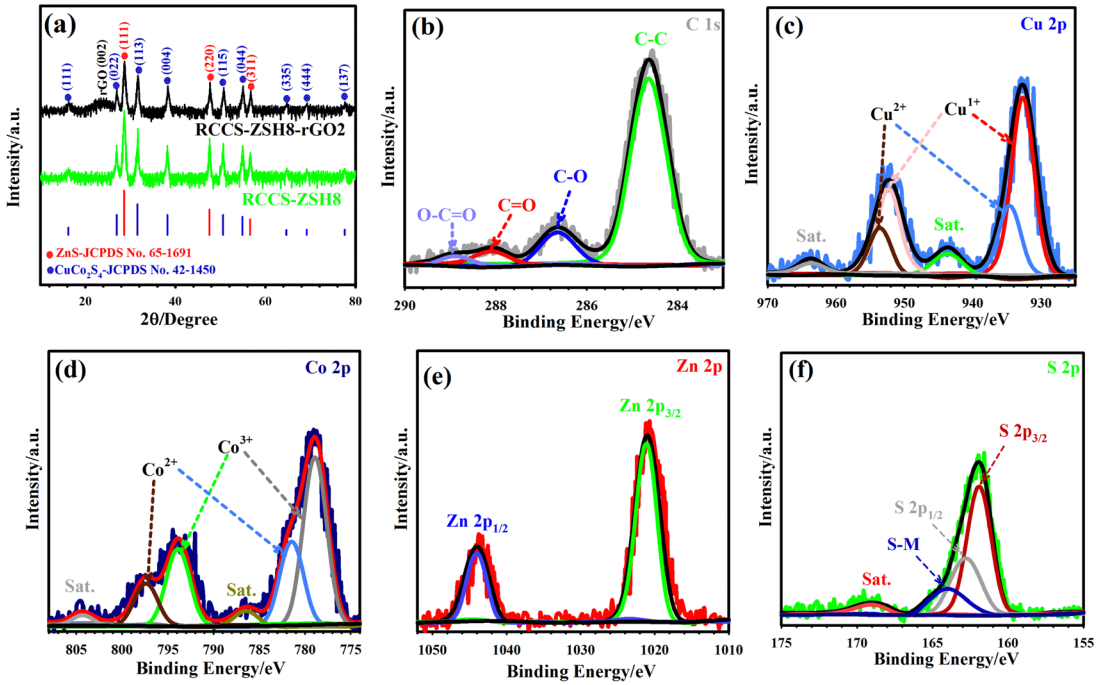

Fig. 4 (a) XRD patterns of the RCCS-ZSH8-rGO (black pattern) and RCCS-ZSH8 (green pattern) samples. (b) C 1s XPS spectra of the RCCS-ZSH8-rGO2 sample. (c) Cu 2p XPS spectra of the RCCS-ZSH8-rGO2 sample. (d) Co 2p XPS spectra of the RCCS-ZSH8-rGO2 sample. (e) Zn 2p XPS spectra of the RCCS-ZSH8-rGO2 sample. (f) S 2p XPS spectra of the RCCS-ZSH8-rGO2 sample.

acted as a protective layer to inhibit the aggregation of the particles.[36,37]

The phase structure of the samples was scrutinized by measuring the XRD pattern of the materials as shown in Fig. 4(a) and Fig. S17, S18 (ESI†). The XRD pattern of CC-G demonstrates that the as-synthesized CC-G was amorphous (Fig. S17(a), ESI†).[57] Besides, the growth of ZIF-8 on CC-G was validated from the XRD pattern which reflects the diffraction peaks of ZIF-8 (Fig. S17(b), ESI†).[58] After the sulfidation of CC-G@ZIF-8 at 140 °C using C_2H_5NS as a sulfidation agent, the XRD pattern of RCCS-ZSH8 displayed diffraction peaks of $CuCo_2S_4$ (JCPDS 42-1450) and ZnS (JCPDS 65-1691) (Fig. 4(a), green pattern). $CuCo_2S_4$ manifested signals at 16.24° (111), 26.95° (022), 31.61° (113), 38.22° (004), 50.56° (115), 54.93° (044), 64.67° (335), 69.12° (444), and 77.58° (137) (Fig. S18(a), ESI†).[30,59] Meanwhile, ZnS reflected three signals at 28.62° (111), 47.55° (220), and 56.6° (311) (Fig. S18(b), ESI†).[60] Besides, the XRD spectrum of RCCS-ZSH8-rGO2 (Fig. 4(a), black pattern) reflects a broad peak located near 24° originating from the rGO layer.[8]

To scrutinize the oxidation states of elements in RCCS-ZSH8-rGO2, XPS analysis was performed. Fig. S19 (ESI†) displays the full-survey spectrum of RCCS-ZSH8-rGO-2, which reflects the presence of S, Cu, Co, C, O, and Zn as constitutive elements. The high-resolution XPS (HR-XPS) spectra of C 1s, Cu 2p, Co 2p, Zn 2p, and S 2p were collected by the Gaussian fitting method. The C 1s pattern represents several binding energy (BE) signals, which belong to C–C (284.68 eV), C–O (286.65 eV), C═O (288.1 eV), and COO (288.91 eV) bonds, respectively (Fig. 4(b)).[24] The C–O and COO bonds reflect lower intensity compared to the C–C bond, demonstrating that graphene oxide was converted into rGO.[37] In the HR-XPS spectrum of Cu 2p, besides two shake-up satellites (indicated as Sat.) situated at 943.55 and 963.65 eV, Cu 2p showed a spin–orbit doublet with signals at 952.55 eV (Cu $2p_{1/2}$) and 932.58 eV (Cu $2p_{3/2}$). The signals at 934.45 and 953.55 eV are indexed to Cu^{2+}, while the signals at 932.52 and 952.12 eV can be assigned to Cu^{+}, respectively (Fig. 4(c)).[35] Likewise, in the HR-XPS spectrum of Co 2p (Fig. 4(d)), Co $2p_{1/2}$ and Co $2p_{3/2}$ were both divided into two obvious peaks, which fitted with Co^{3+} (778.92 and 793.9 eV) and Co^{2+} (781.46 and 797.4 eV), respectively.[32] It is reasonable that Co^{3+} and Co^{2+} co-exist in the as-designed RCCS-ZSH8-rGO2. Meanwhile, two principal signals centered at 1044.3 and 1021.1 eV in the HR-XPS spectrum of Zn 2p (Fig. 4(e)) were assigned to Zn $2p_{1/2}$ and Zn $2p_{3/2}$, respectively, implying the Zn^{2+} oxidation state in RCCS-ZSH8-rGO2.[61] The HR-XPS spectrum of S 2p was also deconvoluted into several signals as shown in Fig. 4(f). The peak at 161.87 eV is related to S^{2-} in RCCS-ZSH8-rGO2, corresponding to $2p_{3/2}$, and the signal at 162.82 eV is assigned to $2p_{1/2}$, while the other signals at 164.1 and 169.1 eV are related to the sulfur–metal (S–M) bond and the satellite peak, respectively.[62–64] The results from XPS and XRD prove that RCCS-ZSH8-rGO2 was successfully synthesized.

The specific surface area (SSA) and porosity are known as critical factors that significantly impact the electrochemical performance of samples.[8,9,13] A large SSA will provide more electroactive sites for the Faradaic reactions, thus leading to high capacity. The SSA and porosity of the RCCS-ZSH8-rGO2, RCCS-ZSH8, CCS-HS, and ZS samples were determined through nitrogen (N_2) adsorption/desorption measurements

and calculated using BET isotherms and BJH pore size distributions. Fig. S20 (ESI†) displays the BET and BJH curves of the RCCS-ZSH8-rGO-2, RCCS-ZSH8, CCS-HS, and ZS samples. The four samples show typical type IV curves with a hysteresis loop, suggesting that the four products possess a mesoporous nature.[65] Also, the BET surface area of RCCS-ZSH8-rGO2 was estimated to be 160.7 $m^2\ g^{-1}$, which was better than that of RCCS-ZSH8 (97.8 $m^2\ g^{-1}$), CCS-HS (62.4 $m^2\ g^{-1}$), and ZnS (48.3 $m^2\ g^{-1}$) (Fig. S20(a), ESI†). The BJH curves of products (Fig. S20(b), ESI†) demonstrate that ZnS, CCS-HS, RCCS-ZSH8, and RCCS-ZSH8-rGO2 reflect a pore size centered at 9.55, 8.9, 7.65, and 6.7 nm, respectively, implying that the products hold mesoporous features.[8,9,13,65] The highly porous structure of RCCS-ZSH8-rGO2 and its resulting high surface area significantly improved the electrolyte penetration and offered a convenient electron diffusion pathway. Therefore, the electrolyte ions could effortlessly move and penetrate the electrode surface, thereby attaining superior supercapacitive performance for RCCS-ZSH8-rGO2.[8,9,13,65]

Through the above characterization tests, it was concluded that the as-made RCCS-ZSH8-rGO2 possesses rich ion transport interfaces and superior conductivity, thanks to the presence of the rGO layer and its exclusive morphology, which can be used as a potential cathode for hybrid supercapacitors. We thus investigated the electrochemical performances of all electrodes in a three-electrode configuration using 6 M KOH as the supporting electrolyte (Fig. 5(a)). Evidence manifests that the specific conductivity of 6 M KOH (62.66×10^{-2} S cm^{-1}) is better compared with other concentrations (1–5 mol L^{-1}) and more desirable for boosting supercapacitive features.[66,67] Thus, 6 M KOH was utilized as an appropriate supporting electrolyte. The higher concentration (>6 M) was not utilized due to the peeling off of the materials from the NF.[66]

Fig. S21(a) (ESI†) presents the CV graphs of the CCG-ZIF, RCCS-ZSH4, RCCS-ZSH6, RCCS-ZSH8, and RCCS-ZSH10 electrodes at 40 mV s^{-1}. The redox peak intensity and integral areas of the optimized RCCS-ZSH8-based-electrode were greater than those of other electrode materials, which demonstrated that RCCS-ZSH8 had better electrochemical characteristics. A similar outcome can be obtained from discharge plots (Fig. S21(b), ESI†), in which RCCS-ZSH8 has a longer discharge time than CCG-ZIF, RCCS-ZSH4, RCCS-ZSH6, and RCCS-ZSH10 electrodes. At 1 A g^{-1}, the RCCS-ZSH8 electrode reflected a maximum capacity of 1050 C g^{-1} whereas the RCCS-ZSH10, RCCS-ZSH6, RCCS-ZSH4, and CC-G@ZIF electrodes revealed 897, 835, 724, and 475 C g^{-1}, respectively (Fig. S21(c), ESI†). Therefore, the RCCS-ZSH8 electrode is considered the optimized electrode material.

The CV and GCD graphs of RCCS-ZSH8-rGO1, RCCS-ZSH8-rGO2, and RCCS-ZSH8-rGO3 tested at 40 mV s^{-1} and 1 A g^{-1}, respectively, are compared in Fig. S22(a) and (b) (ESI†). The RCCS-ZSH8-rGO2 sample manifested a larger enclosed area and a longer discharge time compared with the RCCS-ZSH8-rGO1, and RCCS-ZSH8-rGO3 electrodes, reflecting the higher

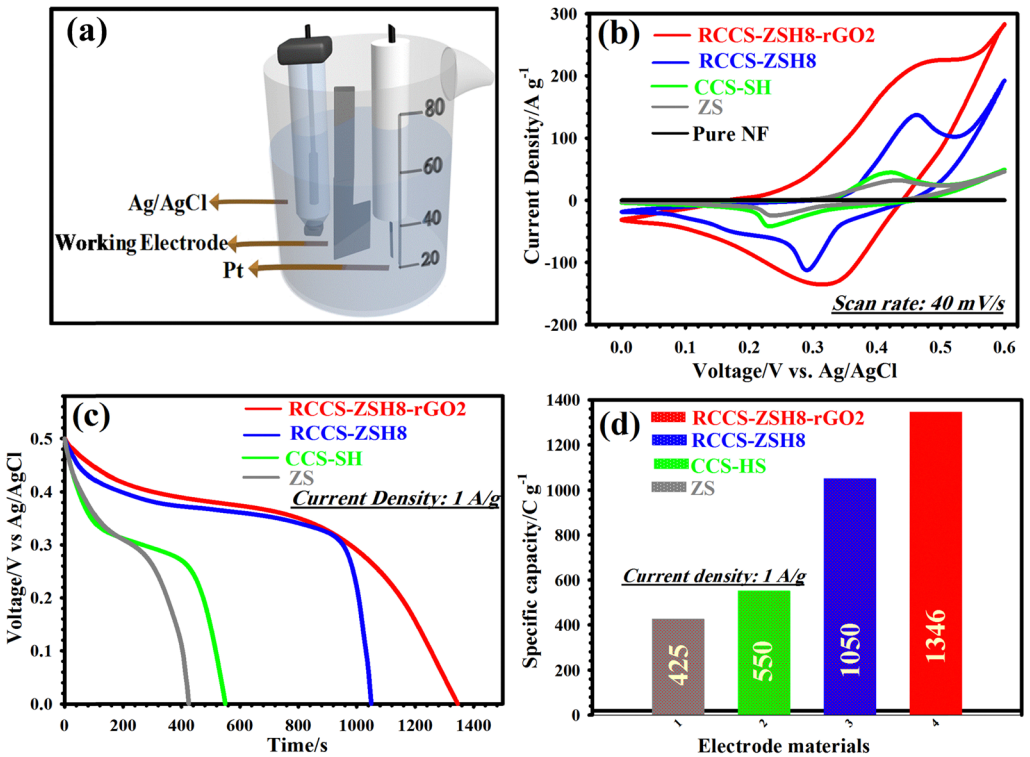

Fig. 5 (a) Schematic illustration of the three-electrode cell. (b) CV curves of the pure nickel foam, ZS, CCS-HS, RCCS-ZSH8, and RCCS-ZSH8-rGO2 electrodes at 40 mV s^{-1}. (c) Discharge curves of the ZS, CCS-HS, RCCS-ZSH8, and RCCS-ZSH8-rGO2 electrodes at 1 A g^{-1}. (d) Specific capacities of ZS, CCS-HS, RCCS-ZSH8, and RCCS-ZSH8-rGO2 electrodes at 1 A g^{-1}.

capacity of the RCCS-ZSH8-rGO2 electrode. At 1 A g^{-1}, RCCS-ZSH8-rGO2 reflected a capacity of 1346 C g^{-1}, whereas the RCCS-ZSH8-rGO1 and RCCS-ZSH8-rGO3 samples demonstrated 1290 and 1255 C g^{-1}, respectively (Fig. S22(c), ESI†).

Fig. 5(b) shows the CV graphs of the pure nickel foam, ZS, CCS-HS, RCCS-ZSH8, and RCCS-ZSH8-rGO2 electrodes at 40 mV s^{-1} from 0.0 to 0.60 V (*vs.* Ag/AgCl). As can be elucidated from Fig. 5(b), pure nickel foam showed no noticeable capacity performance, which proves that the good capacity performances of the electrodes originated from the electroactive materials. The RCCS-ZSH8 electrode reflected a pair of visible redox peaks, verifying the existence of a battery-like electrochemical behavior. During the process, the Faradaic reaction of the RCCS-ZSH8 electrode proceeded as follows:[35,68,69]

$$CuCo_2S_4 + H_2O + OH^- \leftrightarrow CuSOH + 2CuSOH + e^- \quad (6)$$

$$CuSOH + OH^- \leftrightarrow CuSO + 2H_2O + e^- \quad (7)$$

$$CoSOH + OH^- \leftrightarrow CoSO + H_2O + e^- \quad (8)$$

$$ZnS + OH^- \leftrightarrow ZnSOH + e^- \quad (9)$$

$$ZnSOH + OH^- \leftrightarrow ZnSO + H_2O + e^- \quad (10)$$

Besides, the peak current and occupied area in the graph of RCCS-ZSH8-rGO2 are larger than those of the ZS, CCS-HS, and RCCS-ZSH8 electrodes, verifying the high capacity of RCCS-ZSH8-rGO2 due to the good synergistic effect between RCCS-ZSH8 and rGO sheets.[70] Besides, a porous ZnS shell present on the surface of CCS-HS played a critical role in improving the redox reactions by easing the interaction between the electrode and electrolyte to store a large amount of charge.[71] Also, the discharge plots of the as-made electrodes displayed a similar tendency as reflected in Fig. 5(c). The RCCS-ZSH8-rGO2 electrode manifested a longer discharge time compared to ZS, CCS-HS, and RCCS-ZSH8, illustrating its better supercapacitive properties over other electrodes. At 1 A g^{-1}, capacities of 1346, 1050, 550, and 425 C g^{-1} for the RCCS-ZSH8-rGO2, RCCS-ZSH8, CCS-HS, and ZS electrodes, respectively, were obtained (Fig. 5(d)).

EIS is an essential measure for investigating the inherent electrochemical properties of electrode materials.[8,9] Accordingly, EIS was carried out, and the Nyquist graphs of the ZS, CCS-HS, RCCS-ZSH8, and RCCS-ZSH8-rGO2 samples are shown in Fig. 6(a). The EIS results were fitted using Z-view software. Also, the pertinent equivalent circuit is depicted in Fig. 6(a) (inset). In the equivalent circuit, R_{ct} indicates the charge transfer resistance, which is obtained from the semicircle's diameter in the high-frequency zone.[71] The intercept of the Nyquist graphs on the *X*-axis is referred to as R_s, indicating the inherent resistance between the active materials and electrolyte.[71] In the low-frequency area, the slope of the line refers to the Warburg impedance (*W*), which is associated with the diffusion resistance of the ions near the surface of active materials during redox processes.[72] From Fig. 6(a), it can be

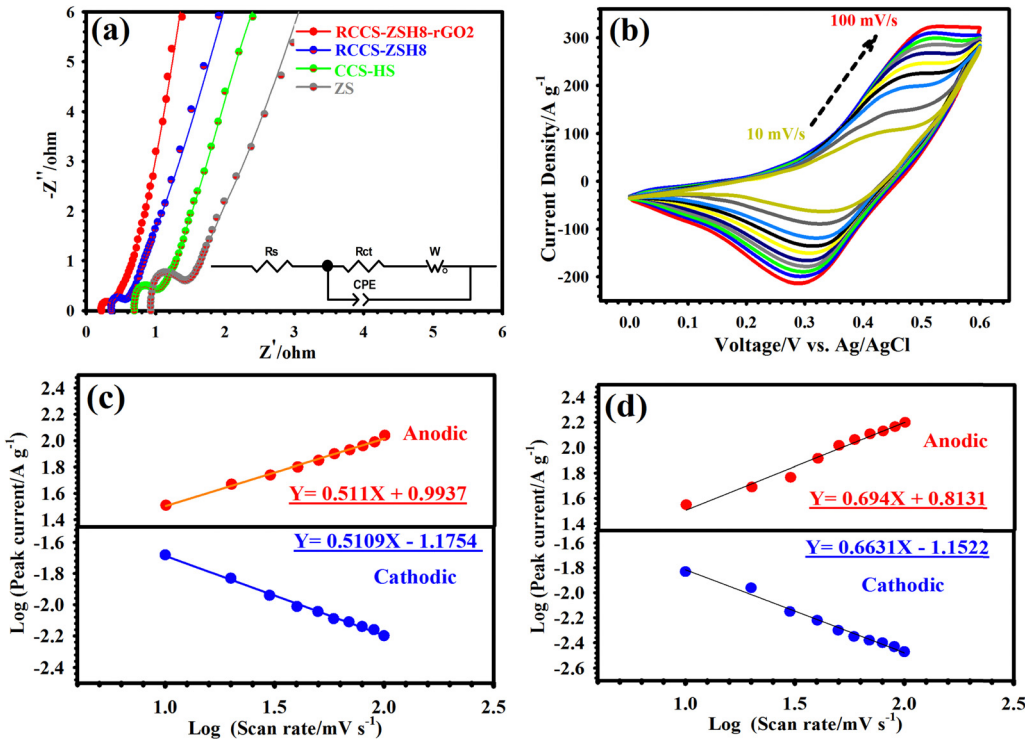

Fig. 6 (a) Nyquist plots of the ZS, CCS-HS, RCCS-ZSH8 and RCCS-ZSH8-rGO2 electrodes (the inset shows the equivalent circuit model and magnified Nyquist curves). (b) CV curves of the RCCS-ZSH8-rGO2 electrode from 10 to 100 mV s^{-1}. (c) Linear relation between the plot of the logarithm (*i*) *versus* logarithm (υ) of the RCCS-ZSH8 electrode. (d) Linear relation between the plot of the logarithm (*i*) *versus* logarithm (υ) of the RCCS-ZSH8-rGO2 electrode.

observed that the RCCS-ZSH8-rGO2 electrode had a lower R_s (0.20 Ω) than RCCS-ZSH8 (0.36 Ω), CCS-HS (0.70 Ω) and ZS (0.92 Ω), signifying its higher conductivity. In the zoomed view of Nyquist curves, the RCCS-ZSH8-rGO2 electrode showed a smaller R_{ct} (0.36 Ω) compared to RCCS-ZSH8 (0.52 Ω), CCS-HS (1.0 Ω) and ZS (1.9 Ω), indicating a faster charge transfer kinetics, which is associated with the highly porous nature of RCCS-ZSH8-rGO2 and the presence of rGO in the sample. As compared to RCCS-ZSH8, CCS-HS, and ZS, the RCCS-ZSH8-rGO2 electrode reflected a vertical line with a larger slope, verifying a lower diffusion resistance.[71,72] Based on the EIS test, it can be concluded that the RCCS-ZSH8-rGO2 electrode presents low R_s and R_{ct}, which is strong evidence for the appropriate selection of the RCCS-ZSH8-rGO2 electrode as an effective cathode material.

The detailed study of the CV plots related to RCCS-ZSH8-rGO2 was performed by varying the sweep speeds from 10 to 100 mV s^{-1} as represented in Fig. 6(b). As reflected in Fig. 6(b), whether the sweep speed was 10 mV s^{-1} or 100 mV s^{-1}, a couple of redox peaks in CV plots were observed, indicating the low internal resistance and good electrochemical reversibility of RCCS-ZSH8-rGO2.[73] As indicated in Fig. 5(b), clear shifts in the positions of cathodic/anodic peaks toward negative/positive voltages, respectively, were observed as the sweep speed was increased owing to the polarization effect.[73] In addition, the CV curves of other electrodes are shown in Fig. S23 (ESI†).

To investigate the comprehensive rate-limiting mechanism (surface-controlled capacity and diffusion-controlled capacity) of the electrodes, the power-law (eqn (11)) can be used to expose the relationship between the peak current (*ip*) and sweep speeds (υ):[12,74,75]

$$\log ip = \log a + b\log(\upsilon) \quad (11)$$

Here, *b* and *a* represent the adjustable parameters. The *b*-value specifies the slope of the line, and it can be obtained by drawing the logarithm of peak current against the logarithm of sweep speed under the constant voltage. Generally, *b* values of 0.5 and 1 signify the diffusion-controlled (battery-type) and surface-controlled (capacitive-type) contribution, respectively. Accordingly, Fig. 6(c) illustrates that the slopes of the cathodic and anodic peaks of the RCCS-ZSH8 electrode were 0.5109 and 0.511, respectively, demonstrating strong evidence for the battery-type behavior of the RCCS-ZSH8.[75] As evidenced in Fig. 6(d), the *b* values of RCCS-ZSH8-rGO2 based on the corresponding reduction (cathodic) and oxidation (anodic) peaks are 0.6631 and 0.694, respectively. The calculated *b* values of RCCS-ZSH8-rGO2 are higher than the *b* values of RCCS-ZSH8, which indicates that the redox reactions of RCCS-ZSH8-rGO2 reflected both surface-controlled and diffusion-controlled kinetics due to the EDLC behavior of the rGO layer. The *b* values of CCS-HS based on the corresponding cathodic and anodic peaks are 0.5031 and 0.5016, respectively. Besides, the *b* values for the cathodic and anodic peaks of the ZS electrode are 0.576 and 0.5716, respectively (Fig. S24, ESI†). The obtained *b*-values for the CCS-HS and ZS electrodes are closer to 0.50, indicating that the energy storage mechanism in the CCS-HS and ZS electrodes is battery-type. Also, the energy storage mechanism of the electric double layer exists in rGO.

The capacitive contribution to the total capacity of the RCCS-ZSH8-rGO2 can be quantitatively analyzed by using the following formula.[37]

$$i = k_1\nu + k_2\nu^{1/2} \quad (12)$$

in which $k_2\nu^{1/2}$ and $k_1\nu$ present the diffusion-controlled and capacitive contributions, respectively. The capacitive contributions for the total capacity of the RCCS-ZSH8-rGO2 and RCCS-ZSH8-based electrodes from 10 to 100 mV s^{-1} are revealed in Fig. S25 (ESI†). As reflected in Fig. S25(a) (ESI†), a diffusion-controlled contribution of 78.6% at 10 mV s^{-1} is shown for RCCS-ZSH8-rGO2, and it decreases to 17.8% at 100 mV s^{-1}. For RCCS-ZSH8, a higher diffusion-controlled contribution of 87.3% at 10 mV s^{-1} is obtained (Fig. S25(b), ESI†), and this value is reduced to 28.5% at 100 mV s^{-1}. These obtained results prove that the charge storage behavior of the RCCS-ZSH8-rGO2 and RCCS-ZSH8 depends on the diffusion-controlled process. Also, the RCCS-ZSH8-rGO2 electrode possesses higher capacitive contributions than the RCCS-ZSH8, demonstrating that the wrapping of the rGO2 sheets is beneficial to accelerate the electrode kinetics, thus improving the charge storage of the composite electrodes.[37]

The energy storage potentiality of the as-prepared electrodes was further verified using GCD tests under diverse current densities (1, 2, 4. 8, 16, and 32 A g^{-1}). The GCD graphs of the RCCS-ZSH8-rGO2 electrode from 1 to 32 A g^{-1} are represented in Fig. 7(a). It can be detected that the noticeable voltage plateaus discovered in the GCD plots matched well with the CV graphs. This result also affirms that the RCCS-ZSH8-rGO2 undergoes a Faradaic reaction.[73,74] Furthermore, the charging and discharging times at all current densities were almost identical, corroborating the impressive Coulombic efficiency, outstanding rate performance, and excellent reversible Faradaic reactions of the RCCS-ZSH8-rGO2 electrode.[12,74] Additionally, the GCD tests of the other electrodes are shown in Fig. S26 (ESI†).

The specific capacities of ZS, CCS-HS, RCCS-ZSH8, and RCCS-ZSH8-rGO2 were carefully calculated (Fig. 7(b)). The observed capacities of the RCCS-ZSH8-rGO2 electrode computed from the GCD curves were 1346, 1326, 1293, 1234, 1194.5, and 1165.6 C g^{-1} at 1, 2, 4, 8, 16, and 32 A g^{-1}, respectively, which were better than those of RCCS-ZSH8-rGO1, RCCS-ZSH8-rGO3 (Fig. S27(a), ESI†), RCCS-ZSH8, CCS-HS, and ZS (Fig. 7(b)), and superior to those of the reported TMS-based electrodes (Fig. 7(c) and Table S1 in ESI†).[76–82] In detail, the RCCS-ZSH8 electrode manifested capacities of 1050, 1025.5, 990, 925.5, 870.25, and 814.8 C g^{-1} at 1, 2, 4, 8, 16, and 32 A g^{-1}, respectively, which were higher than those of CCG-ZIF, RCCS-ZSH4, RCCS-ZSH6, RCCS-ZSH10 (Fig. S27(b), ESI†), CCS-HS and ZS (Fig. 7(b)) electrodes. Also, the CCS-HS electrode exhibited the capacity values of 550, 500, 450, 395, 350, and 302.5 C g^{-1} at 1, 2, 4, 8, 16, and 32 A g^{-1}, respectively (Fig. 7(b)). Similarly, the ZS exhibited capacity values of 425,

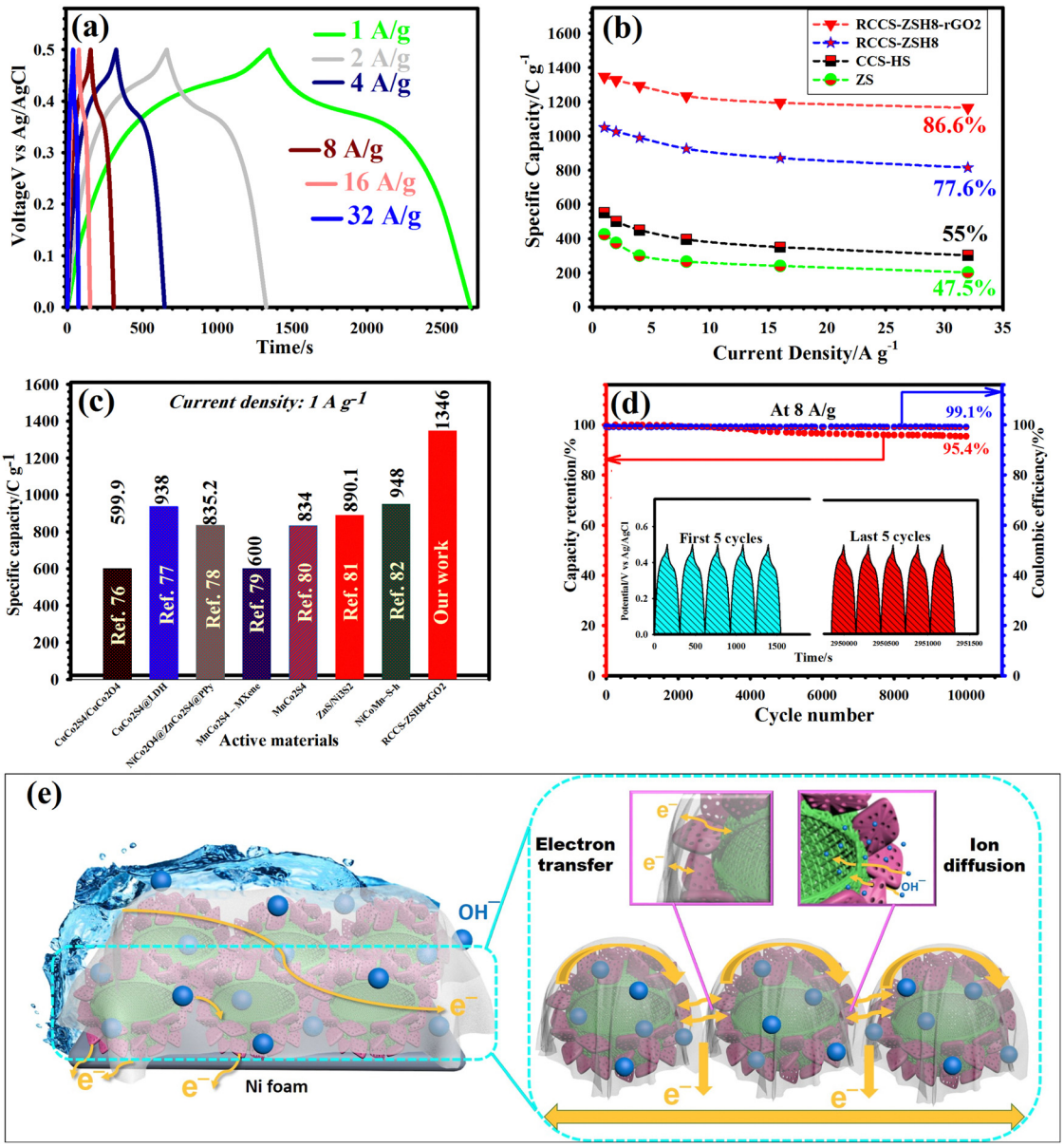

Fig. 7 (a) GCD profiles of the RCCS-ZSH8-rGO2 electrode from 1 to 32 A g^{-1}. (b) Specific capacities *vs.* current densities of the ZS, CCS-HS, RCCS-ZSH8, and RCCS-ZSH8-rGO2 electrodes. (c) Comparison of capacity values of RCCS-ZSH8-rGO2 with the previous literature. (d) Longevity and Coulombic efficiency of the RCCS-ZSH8-rGO2 at 8 A g^{-1} (the inset depicts the first and last 5 GCD cycles). (e) Schematic representation of the working mechanism of RCCS-ZSH8-rGO2 base-electrode.

375, 300, 265, 240, and 201.9 C g^{-1} at 1, 2, 4, 8, 16, and 32 A g^{-1}, respectively (Fig. 7(b)). Even at 32 A g^{-1}, the RCCS-ZSH8-rGO2 electrode maintained 86.6% of its initial capacity, which is higher than that of RCCS-ZSH8-rGO1 (83.8%), RCCS-ZSH8-rGO3 (80.2%) (Fig. S27(a), ESI†), RCCS-ZSH8 (77.6%), CCS-HS (55%), and ZS (47.5%) (Fig. 7(b)).

The excellent capacities and impressive rate capability of the RCCS-ZSH8-rGO2 electrode can be closely related to the effective cooperation between RCCS-ZSH8 and the rGO layer, which enlarges the SSA, enhances conductivity, and provides extra pseudocapacitance for the RCCS-ZSH8-rGO2.[10,83] In the RCCS-ZSH8-rGO2 electrode, the rGO layer can improve the SSA and conductivity and the CCS-HS electrode can provide more active sites and ZS can promote rapid electron and ion transportation through voids of porous ZnS.[36,37,83]

Moreover, the cyclability of samples is another key parameter to evaluate the feasibility of the prepared electrode materials for practical applications. Accordingly, the longevity of all electrode materials was evaluated by performing sequential GCD cycles at 8 A g^{-1}, and the obtained plots are shown in Fig. 7(d) and Fig. S28 (ESI†). The RCCS-ZSH8-rGO2 electrode preserves 95.4% of its capacity after 10 000 cycles (Fig. 7(d)), while the other samples such as RCCS-ZSH8-rGO1, RCCS-ZSH8-rGO3, RCCS-ZSH8, RCCS-ZSH10, RCCS-ZSH6, RCCS-ZSH4,

CCS-HS, CCG-ZIF, and ZS retain 93.1%, 90.6%, 84.2%, 80.5%, 78.5%, 74.5%, 67.6%, 55.6%, and 53.2%, respectively (Fig. S28, ESI†). Also, the RCCS-ZSH8-rGO2 revealed a Coulombic efficiency of 99.1% at the end of the longevity test, signifying the good reversibility nature of RCCS-ZSH8-rGO2 (Fig. 7(d)). The inset in Fig. 7(d) represents the first and last 5 successive GCD cycles for RCCS-ZSH8-rGO2. There was no clear transmutation in the shape of graphs after the durability test, revealing the splendid cyclability of RCCS-ZSH8-rGO2. The electrical conductivity of the RCCS-ZSH8-rGO2 electrode after the longevity test was also investigated by the EIS test (Fig. S29, ESI†). As demonstrated in Fig. S29 (ESI†), a negligible increase in R_{ct} and R_s values after the durability test revealed its rapid charge transportation and good electrochemical conductivity. To further confirm the longevity of RCCS-ZSH8-rGO2, the XRD test was carried out to explore the crystalline nature after the durability test and the obtained patterns are manifested in Fig. S30 (ESI†). As depicted in Fig. S30 (ESI†), there was no fundamental change in the diffraction peaks of RCCS-ZSH8-rGO2 after the longevity test, which indicates that there was no phase change in RCCS-ZSH8-rGO2 even after the longevity test. Moreover, after 10 000 cycles, the morphological studies of RCCS-ZSH8-rGO2 were carried out by performing FE-SEM and TEM (Fig. S31, ESI†). As represented in Fig. S31 (ESI†), the morphology of RCCS-ZSH8-rGO2 did not exhibit any clear aggregation, transfiguration, or collapse, and the RCCS-ZSH8 particles were still encapsulated within the rGO network proving the good structural stability. The remarkable longevity of RCCS-ZSH8-rGO2 results from the high synergistic interaction between rGO, CCS-HS, and ZnS in the RCCS-ZSH8-rGO2 material. The RCCS-ZSH8 electrode acts as a robust skeleton, creating a structural foundation, while the rGO network protects the RCCS-ZSH8, providing good structural stability. Accordingly, the constructive contribution of the rGO, CCS-HS, and ZnS electrode results in enhanced durability.[10,83]

The superb supercapacitive performance of the RCCS-ZSH8-rGO2 electrode can be related to the following characteristics: (1) the wrapping of the rGO network bridges each RCCS-ZSH8 particles together to create a 3D conductive texture (Fig. 7(e)), accelerating the electron transport and thus promoting the fast electrode reactions;[36,37] (2) the rGO network effectively serves as the spacer, effectively inhibiting the aggregation of RCCS-ZSH8 particles, which is beneficial to the penetration of the KOH electrolyte within the electrode, thus increasing the ion diffusion speed within the electrode;[36,37] (3) the good conductivity of the rGO sheets created an expressway for the rapid transfer of electrons, beneficial in reducing the internal resistance and achieving a high supercapacitive performance;[70] (4) the porous/hollow structure with a large surface area is beneficial for increasing the number of electroactive sites and shortening the ion/electron transport paths;[84] (5) the synergistic effect between rGO, CCS-HS and ZnS is advantageous for the enhancement of conductivity and electrochemical active sites, thus achieving high capacity and rate capability;[70,83,84] (6) the introduction of ZnS into CCS-HS could result in increased conductivity and creation of the new active sites, allowing for richer Faradaic redox reactions and resulting in a high capacity;[83,84] and (7) the S atom that is introduced into rCCS-ZSH8-rGO2 plays a vital role in the electrochemical reaction in boosting the conductivity and electrochemical stability of the material.[85]

The CV and GCD tests of the AC were also carried out, as shown in Fig. S32 (ESI†). The capacitance values at 1, 2, 4, 8, 16, and 32 A g^{-1} for the AC@nickel foam were 185.5, 182, 176, 170, 156, and 136 F g^{-1}, respectively.

Inspired by the excellent supercapacitive properties of the as-made RCCS-ZSH8-rGO2 material, an RCCS-ZSH8-rGO2-based hybrid supercapacitor was fabricated for verifying the practical application of the RCCS-ZSH8-rGO2 electrode. Accordingly, we assembled a hybrid supercapacitor (RCCS-ZSH8-rGO2//AC) by sandwiching AC with RCCS-ZSH8-rGO2, as depicted schematically in Fig. 8.

The separate CV graphs of RCCS-ZSH8-rGO2 and AC (Fig. 9(a)) with different voltage ranges were measured in a three-electrode cell at 100 mV s^{-1}. As illustrated in Fig. 9(a), RCCS-ZSH8-rGO2 and AC can be perfectly utilized as cathode and anode electrodes owing to the well-matched charge storage capability. To further confirm this, comparative CV graphs of the RCCS-ZSH8-rGO2//AC were obtained at 20 mV s^{-1} within the voltage range of 0 to 1.7 V (Fig. 9(b)). As demonstrated in Fig. 9(b), beyond the voltage window of 1.6 V, there was a polarization paradox because of the oxygen evolution reactions.[73] Hence, the optimal and stable working voltages of the RCCS-ZSH8-rGO2//AC electrode were set to 0–1.6 V. Fig. 9(c) reveals that the assembled RCCS-ZSH8-rGO2//AC demonstrated nearly symmetric GCD graphs at 1 A g^{-1} with operating voltage windows as high as 1.6 V, signifying that the RCCS-ZSH8-rGO2//AC possessed good Coulombic efficiency.[86] In addition, the linear increase in capacities with respect to the voltage windows demonstrates that RCCS-ZSH8-rGO2 and AC electrodes in RCCS-ZSH8-rGO2//AC were effectively exploited for electrochemical interactions (Fig. 9(d)).[87]

For comparison, we also prepared an RCCS-ZSH8-based hybrid supercapacitor (RCCS-ZSH8//AC), and electrochemical data were collected for both devices. Fig. 10(a) displays the CV patterns of the RCCS-ZSH8-rGO2//AC and RCCS-ZSH8//AC devices at 40 mV s^{-1}. As highlighted in Fig. 10(a), RCCS-ZSH8-rGO2//AC exhibited a larger enclosed internal area than the RCCS-ZSH8//AC, implying its better energy-storage capacity. Furthermore, the GCD patterns of RCCS-ZSH8-rGO2//AC and RCCS-ZSH8//AC devices at 1 A g^{-1} are displayed in Fig. 10(b). It can be found that RCCS-ZSH8-rGO2//AC presents a longer discharging time than RCCS-ZSH8//AC, signifying the higher capacity of the RCCS-ZSH8-rGO2//AC. This result is well-consistent with the CV analysis. Simultaneously, the estimated capacities of these devices at 1 A g^{-1} are plotted in Fig. 10(c). At 1 A g^{-1}, the RCCS-ZSH8-rGO2//AC electrode possesses a capacity of 289 C g^{-1}, obviously better than that of RCCS-ZSH8//AC (223 C g^{-1}), further confirming its higher capacity.

Fig. 10(d) displays the CV profiles of the RCCS-ZSH8-rGO2//AC recorded by varying the sweep speeds from 10 to 100 mV s^{-1}.

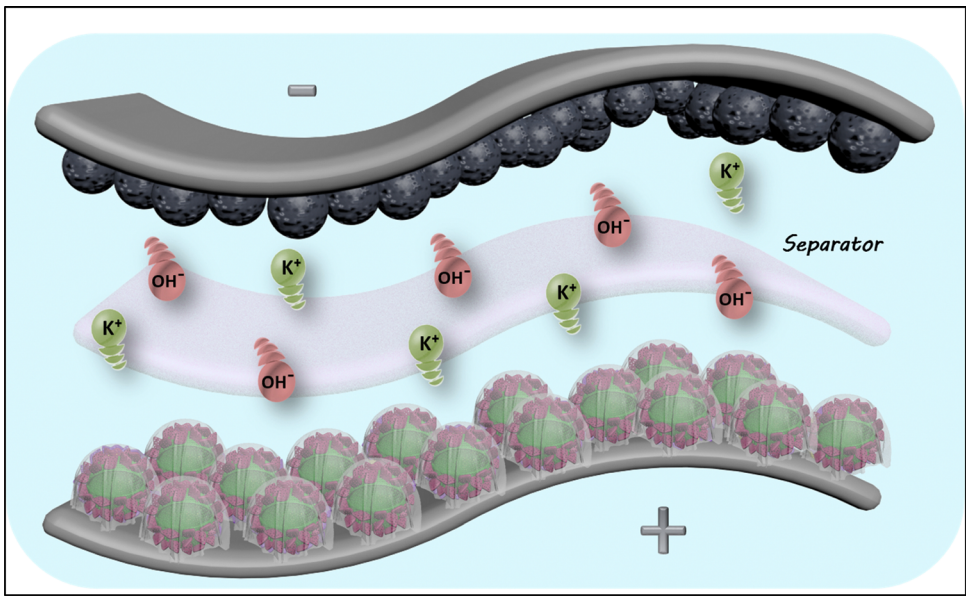

Fig. 8 Schematic illustration of RCCS-ZSH8-rGO2//AC made of RCCS-ZSH8-rGO2 (cathode electrode) and AC (anode electrode).

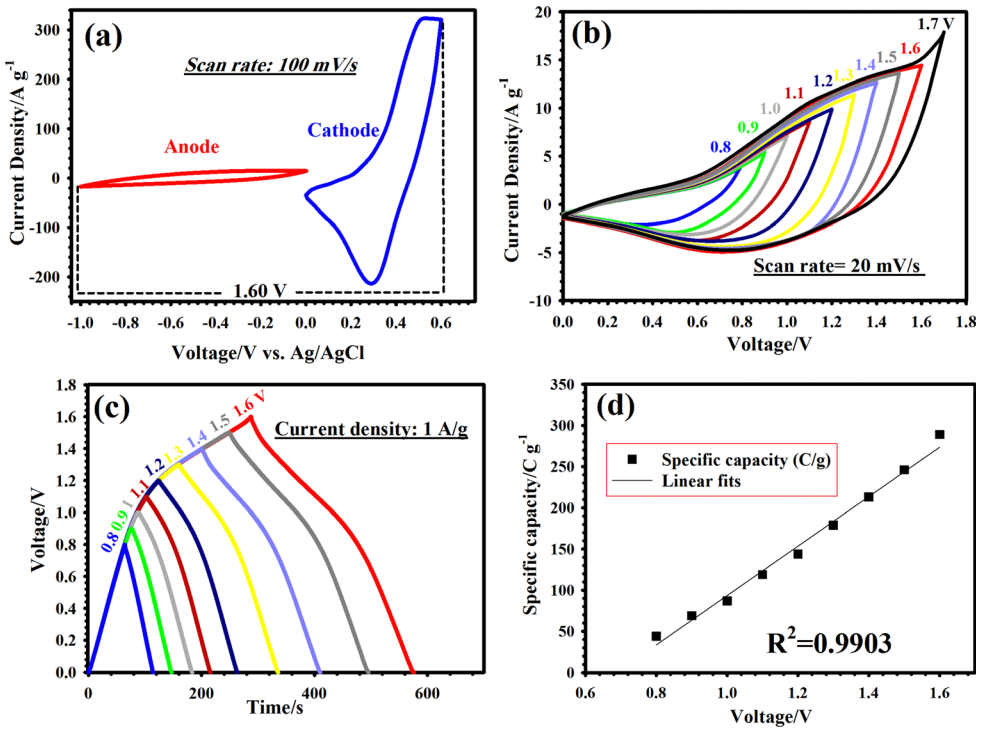

Fig. 9 (a) CVs of AC and RCCS-ZSH8-rGO2 at 100 mV s^{-1} in a three-electrode cell. (b) CV and (c) GCD plots of RCCS-ZSH8-rGO2//AC measured in several voltage windows at a scan rate of 20 mV s^{-1} and a current density of 1 A g^{-1}, respectively. (d) Estimated specific capacity plots based on the voltage windows for RCCS-ZSH8-rGO2//AC at 1 A g^{-1}.

Note that all graphs still preserved their shape even upon increasing the sweep speed to 100 mV s^{-1}, ensuring the outstanding rate performance of our device. In addition, the CV plots conserved the mutual contribution from non-Faradaic and Faradaic performance in all scans, corroborating the Faradaic contribution from RCCS-ZSH8-rGO2 and the capacitive electric double-layer capacitor (EDLC) contribution due to activated carbon. Also, the CV graphs of the RCCS-ZSH8//AC at the same sweep speeds of 10 to 100 mV s^{-1} are presented in Fig. S33(a) (ESI†).

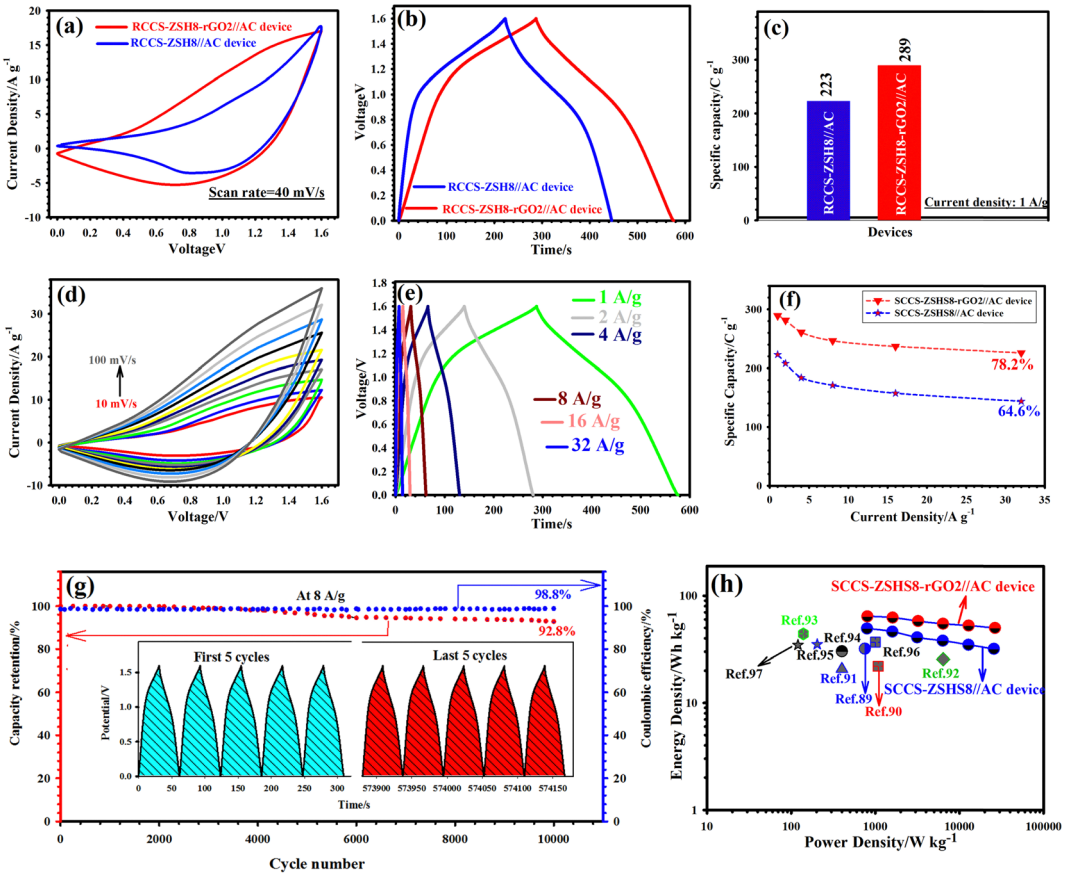

Fig. 10 (a) CV curves of the RCCS-ZSH8//AC and RCCS-ZSH8-rGO2//AC devices at 40 mV s^{-1}. (b) GCD curves of the RCCS-ZSH8//AC and RCCS-ZSH8-rGO2//AC devices at 1 A g^{-1}. (c) Specific capacities of RCCS-ZSH8//AC and RCCS-ZSH8-rGO2//AC devices at 1 A g^{-1}. (d) CV plots of the RCCS-ZSH8-rGO2//AC at various sweep speeds of 10–100 mV s^{-1}. (e) GCD plots of the RCCS-ZSH8-rGO2//AC at various current densities of 1–32 A g^{-1}. (f) Specific capacity *vs.* current density of the RCCS-ZSH8//AC and RCCS-ZSH8-rGO2//AC devices. (g) Durability and coulombic efficiency of the RCCS-ZSH8-rGO2//AC at 8 A g^{-1} (the inset shows the first and last 5 GCD cycles). (h) The comparison of the RCCS-ZSH8-rGO2//AC device's Ragone plot with those of various devices.

Fig. 10(e) manifests the GCD graphs of the RCCS-ZSH8-rGO2//AC electrode from 1 to 32 A g^{-1}. The good symmetry of the obtained curves for the RCCS-ZSH8-rGO2//AC electrode implies high Coulombic efficiency and rapid reversible charge/discharge ability.[85–88] In contrast, the GCD plots of RCCS-ZSH8//AC from 1 to 32 A g^{-1} are displayed in Fig. S33(b) (ESI†). Fig. 10(f) represents the capacities of the RCCS-ZSH8-rGO2//AC device in comparison with the RCCS-ZSHS8//AC device for all current densities. The RCCS-ZSH8-rGO//AC delivered capacities of 289, 281.3, 260.8, 246.4, 236.8, and 226 C g^{-1} at 1, 2, 4, 8, 16, and 32 A g^{-1}, respectively. Also, the estimated specific capacities of the RCCS-ZSH8//AC device were 223, 208, 184, 171.2, 157.6, and 144.1 C g^{-1} at 1, 2, 4, 8, 16, and 32 A g^{-1}, respectively. Even though the current density was enhanced by 32-fold, the RCCS-ZSH8-rGO2//AC electrode maintained 78.2% of its initial capacity, which is higher than that of RCCS-ZSH8//AC (64.6%).

To appraise the recyclability and Coulombic efficiency of the RCCS-ZSH8-rGO2//AC device, an uninterrupted GCD test was performed within a voltage window of 0–1.6 V at 8 A g^{-1}, as sketched in Fig. 10(g). After 10 000 cycles, 92.8% of the initial capacity was retained, implying the outstanding recyclability of the RCCS-ZSH8-rGO2//AC electrode. In addition, it was noticed that our device presented a Coulombic efficiency of 98.8% at the end of the longevity test. Fig. 10(g) (inset) also highlights the first and last 5 cycles of the GCD plots, manifesting the good longevity of the RCCS-ZSH8-rGO2//AC. In addition, the RCCS-ZSH8//AC reflects an 84.4% capacity retention, and its Coulomb efficiency was 95.5% (Fig. S33(c), ESI†).

Energy/power densities are critical parameters of the energy storage performance of supercapacitors. Fig. 10(h) reflects the energy/power densities of the RCCS-ZSH8-rGO//AC and RCCS-ZSH8//AC in the form of a Ragone plot. The estimated energy densities of the RCCS-ZSH8-rGO//AC electrode were 64.2, 62.5, 57.95, 54.75, 52.6, and 50.2 Wh kg^{-1} at 1, 2, 4, 8, 16, and 32 A g^{-1}, while the delivered power densities were 802.5, 1602.6, 3220, 6367, 12 830, and 26 422 W kg^{-1}. Besides, the energy densities of the RCCS-ZSH8//AC electrode were 49.4, 46.2, 40.8, 38, 34.8, and 32 W h kg^{-1} at power densities of 796, 1593.1, 3138, 6330, 12 770, and 25 600 W kg^{-1}, respectively. The RCCS-ZSH8-rGO2//AC electrode revealed better performance compared with RCCS-ZSH8-//AC and many TMS-based

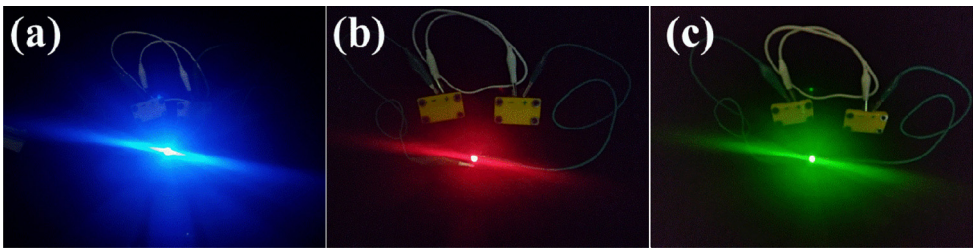

Fig. 11 (a) Photograph of a blue LED with two RCCS-ZSH8-rGO2//AC devices. (b) Photograph of a red LED with two RCCS-ZSH8-rGO2//AC devices. (c) Photograph of a green LED with two RCCS-ZSH8-rGO2//AC devices.

devices.[89–97] For comparison, Table S1 (ESI†) highlights the comparative energy densities of the previous devices.

Eventually, divulging the good energy capability of RCCS-ZSH8-rGO2//AC, it was implemented for practical applications as the energy power source. Therefore, two RCCS-ZSH8-rGO2//AC devices were connected in series to achieve the desired voltage, and after being charged, the blue, red, and green LEDs (light-emitting diodes) were lit with copious intensity (Fig. 11 and Video S1 in ESI†). All of the above results confirm that the as-assembled RCCS-ZSH8-rGO2//AC electrode harvests good energy density without compromising the cycling stability and power delivery, displaying its potential for practical application in hybrid supercapacitors.

Conclusions

In summary, we report the synthesis and delicate design of raspberry-like $CuCo_2S_4$@ZnS hollow particles (RCCS-ZSH) through a facile solution growth, and sulfidation strategy, in which $CuCo_2S_4$ hollow nanospheres (CCS-HSs) are confined in the porous ZnS shells. To improve the electrochemical properties of the RCCS-ZSH sample, the RCCS-ZSH particles were well-encapsulated in the rGO network (RCCS-ZSH-rGO) to form a unique nanoarchitecture. Such a unique nanostructure holds the following advantages: (1) ZnS, as a promising material can contribute to a high capacity, (2) the porous and hollow nature of the RCCS-ZSH can enlarge the active electrolyte/material contact area and shorten the ion diffusion path, thus enhancing the electrochemical reaction kinetics; (3) the heterojunction structure of RCCS-ZSH can enhance the reaction kinetics and electrical conductivity; (4) the rGO encapsulated RCCS-ZSH particles can enhance the conductivity by increasing the synergistic interaction between CCS-HS, ZS, and the rGO network; (5) wrapping of the rGO network around RCCS-ZSH particles effectively hinders the aggregation of RCCS-ZSH particles and maintains the structural durability. Therefore, when used as a cathode material for hybrid supercapacitors, the RCCS-ZSH-rGO2 electrode reflects excellent performance with high capacity, attractive rate capability, and long-term durability. Due to the impressive supercapacitive features of RCCS-ZSH-rGO2, a hybrid supercapacitor (RCCS-ZSH-rGO2//AC) with an energy density of 64.2 W h kg^{-1} at 802.5 W kg^{-1} was assembled. Therefore, it is firmly believed that this research can be easily used for the synthesis of other rGO-encapsulated complex hollow nanostructures for realizing next-generation energy storage systems.

Conflicts of interest

The authors declare no competing financial interest.

Acknowledgements

The authors gratefully acknowledge the support for this work by the Research council of Shahid Beheshti University.

References

1 X. Shen, X. Wei, T. Wang, S. Li and H. Li, Solution-processable hierarchical SiNW/PEDOT/MnO_x electrodes for high-performance supercapacitors, *Mater. Chem. Front.*, 2022, **6**, 2894–2904.
2 B. Ameri, A. Mohammadi Zardkhoshoui and S. S. Hosseiny Davarani, An advanced hybrid supercapacitor constructed from rugby-ball-like $NiCo_2Se_4$ yolk–shell nanostructures, *Mater. Chem. Front.*, 2021, **5**, 4725–4738.
3 F. Yang, J. Chu, Y. Cheng, J. Gong, X. Wang and S. Xiong, Hydrothermal Synthesis of NiCo-layered Double Hydroxide Nanosheets Decorated on Biomass Carbon Skeleton for High Performance Supercapacitor, *Chem. Res. Chin. Univ.*, 2021, **37**, 772–777.
4 W. Gao, Y. Li, J. Zhao, Z. Zhang, W. Tang, J. Wang, Z. Wu and Z. Li, Design and Preparation of Graphene/Fe_2O_3 Nanocomposite as Negative Material for Supercapacitor, *Chem. Res. Chin. Univ.*, 2022, **38**, 1097–1104.
5 Z. Yang, X. Kang, B. Zou, X. Yuan, Y. Li, Q. Wu and Y. Guo, Development of the Self-doping Porous Carbon and Its Application in Supercapacitor Electrode, *Chem. Res. Chin. Univ.*, 2022, **38**, 1065–1072.
6 A. Mohammadi Zardkhoshoui and S. S. Hosseiny Davarani, An efficient hybrid supercapacitor based on Zn–Mn–Ni–S@NiSe core–shell architectures, *Sustainable Energy Fuels*, 2021, **5**, 900–913.
7 P. Tiwari and D. Janas, Emergent pseudocapacitive behavior of single-walled carbon nanotube hybrids: a materials perspective, *Mater. Chem. Front.*, 2022, **6**, 2386–2412.
8 A. Mohammadi Zardkhoshoui, S. S. Hosseiny Davarani, M. Maleka Ashtiani and M. Sarparast, Designing an

asymmetric device based on graphene wrapped yolk–double shell $NiGa_2S_4$ hollow microspheres and graphene wrapped FeS_2–$FeSe_2$ core–shell cratered spheres with outstanding energy density, *J. Mater. Chem. A*, 2019, **7**, 10282–10292.

9 A. Mohammadi Zardkhoshoui, M. Maleka Ashtiani, M. Sarparast and S. S. Hosseiny Davarani, Enhanced the energy density of supercapacitors via rose-like nanoporous $ZnGa_2S_4$ hollow spheres cathode and yolk–shell FeP hollow spheres anode, *J. Power Sources*, 2020, **450**, 227691–227699.

10 A. Mohammadi Zardkhoshoui, B. Ameri and S. S. Hosseiny Davarani, Fabrication of hollow $MnFe_2O_4$ nanocubes assembled by CoS_2 nanosheets for hybrid supercapacitors, *Chem. Eng. J.*, 2022, **435**, 135170.

11 C. Tu, X. Li, C. Lu, Q. Luo, T. Li and M. Zhu, A sequential process to synthesize Fe_3O_4@MnO_2 hollow nanospheres for high performance supercapacitors, *Mater. Chem. Front.*, 2022, **6**, 1938–1947.

12 M. Amiri, A. Mohammadi Zardkhoshoui, S. S. Hosseiny Davarani, M. Maghsoudi and M. K. Altafi, A high-performance hybrid supercapacitor by encapsulating binder-less $FeCoSe_2$ nanosheets@$NiCoSe_2$ nanoflowers in a graphene network, *Sustainable Energy Fuels*, 2022, **6**, 3626–3642.

13 A. Mohammadi Zardkhoshoui and S. S. Hosseiny Davarani, Formation of graphene wrapped multi-shelled $NiGa_2O_4$ hollow spheres and graphene-wrapped yolk–shell $NiFe_2O_4$ hollow spheres derived from metal–organic frameworks for high performance hybrid supercapacitors, *Nanoscale*, 2020, **12**, 1643–1656.

14 A. Mohammadi Zardkhoshoui, S. S. Hosseiny Davarani, M. M. Ashtiani and M. Sarparast, High-performance energy storage device based on triple-shelled cobalt gallium oxide hollow spheres and graphene wrapped copper iron disulfide Porous spheres, *ACS Sustainable Chem. Eng.*, 2019, **7**, 7908–7917.

15 X. Hu, S. Liu, Y. Wang, X. Huang, J. Jiang, H. Cong, H. Lin and S. Han, Hierarchical $CuCo_2O_4$@CoS-Cu/Co-MOF core–shell nanoflower derived from copper/cobalt bimetallic metal–organic frameworks for supercapacitors, *J. Colloid Interface Sci.*, 2021, **600**, 72–82.

16 W. Chen, T. Wei, L.-E. Mo, S. Wu, Z. Li, S. Chen, X. Zhang and L. Hu, CoS_2 nanosheets on carbon cloth for flexible all-solid-state supercapacitors, *Chem. Eng. J.*, 2020, **400**, 125856.

17 A. Mohammadi Zardkhoshoui, R. Hayati Monjoghtapeh and S. S. Hosseiny Davarani, Zn–Ni–Se@$NiCo_2S_4$ core–shell architectures: a highly efficient positive electrode for hybrid supercapacitors, *Energy Fuels*, 2020, **34**, 14934–14947.

18 L. Yang, Q. Zhu, K. Yang, X. Xu, J. Huang, H. Chen and H. Wang, A Review on the Application of Cobalt-Based Nanomaterials in Supercapacitors, *Nanomater*, 2022, **12**, 11–18.

19 X. Li, X. Xiao, Q. Li, J. Wei, H. Xue and H. Pang, Metal (M = Co, Ni) phosphate based materials for high-performance supercapacitors, *Inorg. Chem. Front.*, 2018, **5**, 11–28.

20 A. Mohammadi Zardkhoshoui and S. S. Hosseiny Davarani, Construction of complex copper-cobalt selenide hollow structures as an attractive battery-type electrode material for hybrid supercapacitors, *Chem. Eng. J.*, 2020, **402**, 126241–126252.

21 B. Ameri, A. Mohammadi Zardkhoshoui and S. S. Hosseiny Davarani, Engineering of hierarchical $NiCoSe_2$@NiMn-LDH core–shell nanostructures as a high-performance positive electrode material for hybrid supercapacitor, *Sustainable Energy Fuels*, 2020, **4**, 5144–5155.

22 X. Du, J. Sun, R. Wu, E. Bao, C. Xu and H. Chen, Uniform $MnCo_2O_{4.5}$ porous nanowires and quasi-cubes for hybrid supercapacitors with excellent electrochemical performances, *Nanoscale Adv.*, 2021, **3**, 4447–4458.

23 I. Hussain, T. Hussain, S. Yang, Y. Chen, J. Zhou, X. Ma, N. Abbas, C. Lamiel and K. Zhang, Integration of CuO nanosheets to Zn–Ni–Co oxide nanowire arrays for energy storage applications, *Chem. Eng. J.*, 2021, **413**, 127570.

24 Y. A. Haj, J. Balamurugan, N. H. Kim and J. H. Lee, Nitrogen-doped graphene encapsulated cobalt iron sulfide as an advanced electrode for high-performance asymmetric supercapacitors, *J. Mater. Chem. A*, 2019, **7**, 3941–3952.

25 P. Kulkarni, S. K. Nataraj, R. G. Balakrishna, D. H. Nagaraju and M. V. Reddy, Nanostructured binary and ternary metal sulfides: synthesis methods and their application in energy conversion and storage devices, *J. Mater. Chem. A*, 2017, **5**, 22040–22094.

26 S. C. Sekhar, B. Ramulu, S. J. Arbaz, S. K. Hussain and J. S. Yu, One-Pot Hydrothermal-Derived NiS_2–$CoMo_2S_4$ with Vertically Aligned Nanorods as a Binder-Free Electrode for Coin-Cell-Type Hybrid Supercapacitor, *Small Methods*, 2021, **5**, 2100335.

27 C. Li, J. Balamurugan, N. H. Kim and J. H. Lee, Hierarchical Zn–Co–S Nanowires as Advanced Electrodes for All Solid State Asymmetric Supercapacitors, *Adv. Energy Mater.*, 2017, **8**, 1702014.

28 W. He, C. Wang, H. Li, X. Deng, X. Xu and T. Zhai, Ultrathin and Porous Ni_3S_2/$CoNi_2S_4$ 3D-Network Structure for Superhigh Energy Density Asymmetric Supercapacitors, *Adv. Energy Mater.*, 2017, **7**, 1700983.

29 S. Liu, L. Kang, J. Hu, E. Jung, J. Henzie, A. Alowasheeir, J. Zhang, L. Miao, Y. Yamauchi and S. C. Jun, Realizing Superior Redox Kinetics of Hollow Bimetallic Sulfide Nanoarchitectures by Defect-Induced Manipulation toward Flexible Solid-State Supercapacitors, *Small*, 2021, **18**, 2104507.

30 R. Asadi, A. Mohammadi Zardkhoshoui, S. N. Azizi and S. S. Hosseiny Davarani, Designing an Advanced Supercapattery Based on $CuCo_2S_4$@Ni−Mo−S Nanosheet Arrays, *ChemElectroChem*, 2019, **6**, 5984–5992.

31 A. Bahaa, J. Balamurugan, N. H. Kim and J. H. Lee, Metal–organic framework derived hierarchical copper cobalt sulfide nanosheet arrays for high-performance solid-state asymmetric supercapacitors, *J. Mater. Chem. A*, 2019, **7**, 8620–8632.

32 H. You, L. Zhang, Y. Jiang, T. Shao, M. Li and J. Gong, Bubble-supported engineering of hierarchical $CuCo_2S_4$ hollow spheres for enhanced electrochemical performance, *J. Mater. Chem. A*, 2018, **6**, 5265–5270.

33 H. Jia, Y. Cai, Z. Wang, X. Zheng, C. Li, H. Liang, J. Qi, J. Cao, J. Feng and W. Fei, Sea urchin-like $CuCo_2S_4$ microspheres with a controllable interior structure as advanced electrode materials for high-performance supercapacitors, *Inorg. Chem. Front.*, 2020, **7**, 603–609.

34 L. Han, X. Liu, Z. Cui, Y. Hua, C. Wang, X. Zhao and X. Liu, Hierarchical copper cobalt sulfide nanobelt arrays for high performance asymmetric supercapacitors, *Inorg. Chem. Front.*, 2021, **8**, 3025–3036.

35 L. Kang, C. Huang, J. Zhang, M. Zhang, N. Zhang, S. Liu, Y. Ye, C. Luo, Z. Gong, C. Wang, X. Zhou, X. Wu and S. C. Jun, Effect of fluorine doping and sulfur vacancies of $CuCo_2S_4$ on its electrochemical performance in supercapacitors, *Chem. Eng. J.*, 2020, **390**, 124643.

36 M. Amiri, A. Mohammadi Zardkhoshoui and S. S. Hosseiny Davarani, Fabrication of nanosheet-assembled hollow copper–nickel phosphide spheres embedded in reduced graphene oxide texture for hybrid supercapacitors, *Nanoscale*, 2023, **15**, 2806–2819.

37 B. Hu, X. Liu, A. Liu, Y. Ren, Z. Guo, J. Mu, X. Zhang, Z. Zhang, X. Liu and H. Che, Reduced Graphene Oxide Nanosheet-Wrapped Hollow Cobalt Selenide Nanocubes as Electrodes for Supercapacitors, *ACS Appl. Nano Mater.*, 2021, **4**, 13267–13278.

38 K. D. Ikkurthi, S. S. Rao, J.-W. Ahn, C. D. Sunesh and H.-J. Kim, A cabbage leaf like nanostructure of a NiS@ZnS composite on Ni foam with excellent electrochemical performance for supercapacitors, *Dalton Trans.*, 2019, **48**, 578–586.

39 I. Hussain, D. Mohapatra, G. Dhakal, C. Lamiel, S. G. Mohamed, M. S. Sayed and J.-J. Shim, Different controlled nanostructures of Mn-doped ZnS for high-performance supercapacitor applications, *J. Energy Storage*, 2020, **32**, 101767.

40 H. Chen, J. Zhou, Q. Li, S. Zhao, X. Yu, K. Tao, Y. Hu and L. Han, MOF-assisted construction of a Co_9S_8@Ni_3S_2/ZnS microplate array with ultrahigh areal specific capacity for advanced supercapattery, *Dalton Trans.*, 2020, **49**, 10535–10544.

41 A. Mohammadi Zardkhoshoui, B. Ameri and S. S. Hosseiny Davarani, A high-energy-density supercapacitor with multishelled nickel–manganese selenide hollow spheres as cathode and double-shell nickel–iron selenide hollow spheres as anode electrodes, *Nanoscale*, 2021, **13**, 2931–2945.

42 A. Mohammadi Zardkhoshoui and S. S. Hosseiny Davarani, Boosting the energy density of supercapacitors by encapsulating a multi-shelled zinc–cobalt–selenide hollow nanosphere cathode and a yolk–double shell cobalt–iron–selenide hollow nanosphere anode in a graphene network, *Nanoscale*, 2020, **12**, 12476–12489.

43 L. Shen, L. Yu, H. B. Wu, X.-Y. Yu, X. Zhang and X. W. Lou, Formation of nickel cobalt sulfide ball-in-ball hollow spheres with enhanced electrochemical pseudocapacitive properties, *Nat. Commun.*, 2015, **6**, 6694.

44 R. He, S. Li, H. Liu and L. Zhou, Hetero-structured Fe–Cr–O hollow multishelled spheres for stable sodium storage, *Mater. Chem. Front.*, 2022, **6**, 1903–1911.

45 Z. Liu, H. Song, Y. Zhao, R. He, J. Meng, Q. Yu, K. A. Owusu, C. Yu, D. Zhao, L. Zhou and L. Mai, Heterogeneous Contraction-Mediated Asymmetric Carbon Colloids, *ACS Mater. Lett.*, 2019, **1**, 290–296.

46 M. Chen, J. Wang, H. Tang, Y. Yang, B. Wang, H. Zhao and D. Wang, Synthesis of multi-shelled MnO_2 hollow microspheres via an anion-adsorption process of hydrothermal intensification, *Inorg. Chem. Front.*, 2016, **3**, 1065–1070.

47 J. Wang, H. Tang, H. Ren, R. Yu, J. Qi, D. Mao, H. Zhao and D. Wang, pH-Regulated Synthesis of Multi-Shelled Manganese Oxide Hollow Microspheres as Supercapacitor Electrodes Using Carbonaceous Microspheres as Templates, *Adv. Sci.*, 2014, **1**, 1400011.

48 B. Ruyi, M. Dan, W. Jiangyan, Y. Ranbo and W. Dan, Hollow Nanostructures for Surface/Interface Chemical Energy Storage Application, *Acta Chim. Sin.*, 2020, **78**, 1200.

49 M. Zeeshan and M. Shahid, State of the art developments and prospects of metal–organic frameworks for energy applications, *Dalton Trans.*, 2022, **51**, 1675–1723.

50 Y. Jiao, J. Pei, D. Chen, C. Yan, Y. Hu, Q. Zhang and G. Chen, Mixed-metallic MOF based electrode materials for high performance hybrid supercapacitors, *J. Mater. Chem. A*, 2017, **5**, 1094–1102.

51 X. Han, K. Tao, D. Wang and L. Han, Design of a porous cobalt sulfide nanosheet array on Ni foam from zeolitic imidazolate frameworks as an advanced electrode for supercapacitors, *Nanoscale*, 2018, **10**, 2735–2741.

52 S. A. Hira and K. H. Park, Nitrogen-Doped Zeolitic Imidazolate Framework and Particle-Reduced Graphene Oxide Composites as Electrochemical Sensors and Battery-Type Supercapacitors, *ACS Appl. Nano Mater.*, 2021, **4**, 7870–7878.

53 X.-M. Cao and Z.-B. Han, Hollow core–shell ZnO@ZIF-8 on carbon cloth for flexible supercapacitors with ultrahigh areal capacitance, *Chem. Commun.*, 2019, **55**, 1746–1749.

54 R. R. Salunkhe, C. Young, J. Tang, T. Takei, Y. Ide, N. Kobayashi and Y. Yamauchi, A high-performance supercapacitor cell based on ZIF-8-derived nanoporous carbon using an organic electrolyte, *Chem. Commun.*, 2016, **52**, 4764–4767.

55 L. Wan, Y. Wang, Y. Zhang, C. Du, J. Chen, Z. Tian and M. Xie, FeCoP nanosheets@Ni-Co carbonate hydroxide nanoneedles as free-standing electrode material for hybrid supercapacitors, *Chem. Eng. J.*, 2021, **415**, 128995.

56 S. Wang, B. Y. Guan, X. Wang and X. W. Lou, Formation of Hierarchical Co_9S_8@$ZnIn_2S_4$ Heterostructured Cages as an Efficient Photocatalyst for Hydrogen Evolution, *J. Am. Chem. Soc.*, 2018, **140**, 15145–15148.

57 X. Zhang, Y. Zhou, B. Luo, H. Zhu, W. Chu and K. Huang, Microwave-Assisted Synthesis of $NiCo_2O_4$ Double-Shelled Hollow Spheres for High-Performance Sodium Ion Batteries, *Nano-Micro Lett.*, 2018, **10**, 13–20.

58 A. Schejn, A. Aboulaich, L. Balan, V. Falk, J. Lalevée, G. Medjahdi, L. Aranda, K. Mozet and R. Schneider, Cu^{2+}-doped zeolitic imidazolate frameworks (ZIF-8): efficient and stable catalysts for cycloadditions and condensation reactions, *Catal. Sci. Technol.*, 2015, **5**, 1829–1839.

59 Y. K. Sonia, M. K. Paliwal and S. K. Meher, The rational design of hierarchical CoS_2/$CuCo_2S_4$ for three-dimensional all-solid-state hybrid supercapacitors with high energy density, rate efficiency, and operational stability, *Sustainable Energy Fuels*, 2021, **5**, 973–985.

60 W. Zhan, Y. Yuan, B. Yang, F. Jia and S. Song, Construction of MoS_2 nano-heterojunction via ZnS doping for enhancing in-situ photocatalytic reduction of gold thiosulfate complex, *Chem. Eng. J.*, 2020, **394**, 124866.

61 G. Sun, S. Mao, D. Ma, Y. Zou, Y. Lv, Z. Li, C. He, Y. Cheng and J.-W. Shi, One-step vulcanization of Cd(OH)Cl nanorods to synthesize CdS/ZnS/PdS nanotubes for highly efficient photocatalytic hydrogen evolution, *J. Mater. Chem. A*, 2019, **7**, 15278–15287.

62 H. Zhang, X. Wang, Z. Yang, S. Yan, C. Zhang and S. Liu, Space-Confined Synthesis of Lasagna-like N-Doped Graphene-Wrapped Copper–Cobalt Sulfides as Efficient and Durable Electrocatalysts for Oxygen Reduction and Oxygen Evolution Reactions, *ACS Sustainable Chem. Eng.*, 2020, **8**, 1004–1014.

63 B. X. Li, Z. Tian, H. J. Li, Z. W. Yang, Y. Z. Wang and X. M. Wang, Self-supporting graphene aerogel electrode intensified by $NiCo_2S_4$ nanoparticles for asymmetric supercapacitor, *Electrochim. Acta*, 2019, **314**, 32–39.

64 Y. V. Lim, S. Huang, Q. Wu, D. Kong, Y. Wang, Y. Zhu, Y. Wang, Y.-X. Wang, H.-K. Liu, S.-X. Dou, L. K. Ang and H. Y. Yang, Super Kinetically Pseudocapacitive $MnCo_2S_4$ Nanourchins toward High-Rate and Highly Stable Sodium-Ion Storage, *Adv. Funct. Mater.*, 2020, **30**, 1909702.

65 L. Sun, Z. Xie, A. Wu, C. Tian, D. Wang, Y. Gu, Y. Gao and H. Fu, Hollow CoP spheres assembled from porous nanosheets as high-rate and ultra-stable electrodes for advanced supercapacitors, *J. Mater. Chem. A*, 2021, **9**, 26226–26235.

66 W. Jiang, F. Hu, Q. Yan and X. Wu, Investigation on electrochemical behaviors of $NiCo_2O_4$ battery-type supercapacitor electrodes: the role of an aqueous electrolyte, *Inorg. Chem. Front.*, 2017, **4**, 1642–1648.

67 R. Gilliam, J. Graydon, D. Kirk and S. Thorpe, A review of specific conductivities of potassium hydroxide solutions for various concentrations and temperatures, *Int. J. Hydrogen Energy*, 2007, **32**, 359–364.

68 H. Li, Z. Li, Z. Wu, M. Sun, S. Han, C. Cai, W. Shen, X. Teng, L. Yong and Q. Fu, Enhanced electrochemical performance of $CuCo_2S_4$/carbon nanotubes composite as electrode material for supercapacitors, *J. Colloid Interface Sci.*, 2019, **549**, 105–113.

69 I. Hussain, D. Mohapatra, G. Dhakal, C. Lamiel, M. S. Sayed, S. Sahoo, S. G. Mohamed, J. S. Kim, Y. R. Lee and J.-J. Shim, Uniform growth of ZnS nanoflakes for high-performance supercapacitor applications, *J. Energy Storage*, 2021, **36**, 102408.

70 W. Liu, H. Niu, J. Yang, K. Cheng, K. Ye, K. Zhu, G. Wang, D. Cao and J. Yan, Ternary Transition Metal Sulfides Embedded in Graphene Nanosheets as Both the Anode and Cathode for High-Performance Asymmetric Supercapacitors, *Chem. Mater.*, 2018, **30**, 1055–1068.

71 N. Jayababu and D. Kim, CuCo LDHs Coated CuCoTe Honeycomb-Like Nanosheets as a Novel Anode Material for Hybrid Supercapacitors, *Small*, 2021, **17**, 2102369.

72 P. Li, S. Liu, Y. Mao, H. Yin, S.-M. Chen and X. Liu, Surface Self-Reconstruction and Sulfidation Strategy to Fabricate Flower-Like $NiCo_2S_4$ Hollow Nanospheres: Formation, Storage Mechanism, and Application in Hybrid Supercapacitors, *ACS Appl. Energy Mater.*, 2021, **4**, 9178–9189.

73 K. Li, B. Zhao, H. Zhang, H. Lv, J. Bai, H. Ma, P. Wang, W. Li, J. Si, X. Zhu and Y. Sun, 3D Porous Honeycomb-Like CoN-Ni_3N/N-C Nanosheets Integrated Electrode for High-Energy-Density Flexible Supercapacitor, *Adv. Funct. Mater.*, 2021, **31**, 2103073.

74 Q. Li, Q. Zhang, J. Sun, C. Liu, J. Guo, B. He, Z. Zhou, P. Man, C. Li, L. Xie and Y. Yao, All Hierarchical Core–Shell Heterostructures as Novel Binder-Free Electrode Materials for Ultrahigh-Energy-Density Wearable Asymmetric Supercapacitors, *Adv. Sci.*, 2018, **6**, 1801379.

75 J. Y. Dai, S. B. Singh, N. H. Kim and J. H. Lee, Hierarchical 3D structured nanoporous Co_9S_8@Nix:Moy–Se core–shell nanowire array electrodes for high-performance asymmetric supercapacitors, *J. Mater. Chem. A*, 2021, **9**, 27503–27517.

76 X. Xu, Y. Liu, P. Dong, P. M. Ajayan, J. Shen and M. Ye, Mesostructured $CuCo_2S_4$/$CuCo_2O_4$ nanoflowers as advanced electrodes for asymmetric supercapacitors, *J. Power Sources*, 2018, **400**, 96–103.

77 H.-B. Li, G.-F. Xiao, H.-Y. Zeng, X.-J. Cao, K.-M. Zou and S. Xu, Supercapacitor based on the $CuCo_2S_4$@NiCoAl hydrotalcite array on Ni foam with high-performance, *Electrochim. Acta*, 2020, **352**, 136500.

78 D. Zhao, H. Liu and X. Wu, Bi-interface induced multi-active MCo_2O_4@MCo_2S_4@PPy (M = Ni, Zn) sandwich structure for energy storage and electrocatalysis, *Nano Energy*, 2019, **57**, 363–370.

79 K. Nasrin, K. Subramani, M. Karnan and M. Sathish, $MnCo_2S_4$–MXene: a novel hybrid electrode material for high performance long-life asymmetric supercapattery, *J. Colloid Interface Sci.*, 2021, **600**, 264–277.

80 L. Abbasi, M. Arvand and S. E. Moosavifard, Facile template-free synthesis of 3D hierarchical ravine-like interconnected $MnCo_2S_4$ nanosheet arrays for hybrid energy storage device, *Carbon*, 2020, **161**, 299–308.

81 Y. Zhang, N. Cao, M. Li, S. Szunerits, A. Addad, P. Roussel and R. Boukherroub, Self-template synthesis of ZnS/Ni_3S_2 as advanced electrode material for hybrid supercapacitors, *Electrochim. Acta*, 2019, **328**, 135065.

82 Z. Peng, C. Yang, Y. Hu, F. Bai, W. Chen, R. Liu, S. Jiang and H.-C. Chen, Double-shelled Mn-doped $NiCo_2S_4$ hollow nanowire arrays for high-reactivity hybrid supercapacitors, *Appl. Surf. Sci.*, 2022, **573**, 151561.

83 M. Liang, M. Zhao, H. Wang, J. Shen and X. Song, Enhanced cycling stability of hierarchical $NiCo_2S_4$@$Ni(OH)_2$@PPy core–shell nanotube arrays for aqueous asymmetric supercapacitors, *J. Mater. Chem. A*, 2018, **6**, 2482–2493.

84 Z. Xie, D. Qiu, J. Xia, J. Wei, M. Li, F. Wang and R. Yang, Hollow Biphase Cobalt Nickel Perselenide Spheres Derived

from Metal Glycerol Alkoxides for High-Performance Hybrid Supercapacitors, *ACS Appl. Mater. Interfaces*, 2021, **13**, 12006–12015.

85 S. C. Tang, B. G. Zhu, X. L. Shi, J. Wu and X. K. Meng, General Controlled Sulfidation toward Achieving Novel Nanosheet-Built Porous Square-$FeCo_2S_4$-Tube Arrays for High-Performance Asymmetric All-Solid-State Pseudocapacitors, *Adv. Energy Mater.*, 2017, **7**, 1601985.

86 Q. Li, Interfacial Control of NiCoP@NiCoP Core–Shell Nanoflake Arrays as Advanced Cathodes for Ultrahigh-Energy-Density Fiber-Shaped Asymmetric Supercapacitors, *Small*, 2021, **17**, 2101617.

87 G. Nagaraju, S. C. Sekhar, B. Ramulu and J. S. Yu, High-performance hybrid supercapacitors based on MOF-derived hollow ternary chalcogenides, *Energy Storage Mater.*, 2021, **35**, 750–760.

88 K. Zhang, H.-Y. Zeng, H.-B. Li, S. Xu, S.-B. Lv and M.-X. Wang, Controllable preparation of $CuCo_2S_4$ nanotube arrays for high-performance hybrid supercapacitors, *Electrochim. Acta*, 2022, **404**, 139681.

89 P. Naveenkumar and G. P. Kalaignan, Fabrication of core–shell like hybrids of $CuCo_2S_4$@$NiCo(OH)_2$ nanosheets for supercapacitor applications, *Composites, Part B*, 2019, **17**, 106864.

90 Z. Tian, X. Wang, B. Li, H. Li and Y. Wu, High rate capability electrode constructed by anchoring $CuCo_2S_4$ on graphene aerogel skeleton toward quasi-solid-state supercapacitor, *Electrochim. Acta*, 2019, **298**, 321–329.

91 H. Jia, Y. Song, J. Wu, W. Fu, J. Zhao and X. Liu, A novel P-doped $MnCo_2S_4$ nanoneedles assembled dandelion-like structure for high performance hybrid supercapacitors, *Mater. Lett.*, 2018, **323**, 55–58.

92 K. Nasrin, K. Subramani, M. Karnan and M. Sathish, $MnCo_2S_4$-MXene: a novel hybrid electrode material for high performance long-life asymmetric supercapattery, *J. Colloid Interface Sci.*, 2021, **600**, 264–277.

93 Q. Zhou, J. Huang, C. Li, Z. Lv, H. Zhu and G. Hu, Wrapping $CuCo_2S_4$ arrays on nickel foam with $Ni_2(CO_3)(OH)_2$ nanosheets as a high-performance faradaic electrode, *New J. Chem.*, 2019, **43**, 5904–5913.

94 M. Zhang, H. Du, Z. Wei, X. Zhang and R. Wang, Ultrafast Microwave Synthesis of Nickel–Cobalt Sulfide/Graphene Hybrid Electrodes for High-Performance Asymmetrical Supercapacitors, *ACS Appl. Energy Mater.*, 2021, **4**, 8262–8274.

95 Y. Liu, G. Jiang, Z. Huang, Q. Lu, B. Yu, U. Evariste and P. Ma, Decoration of Hollow Mesoporous Carbon Spheres by $NiCo_2S_4$ Nanoparticles as Electrode Materials for Asymmetric Supercapacitors, *ACS Appl. Energy Mater.*, 2019, **2**, 8079–8089.

96 Y. Chen, T. Liu, L. Zhang and J. Yu, $NiCo_2S_4$ Nanotubes Anchored 3D Nitrogen-Doped Graphene Framework as Electrode Material with Enhanced Performance for Asymmetric Supercapacitors, *ACS Sustainable Chem. Eng.*, 2019, **7**, 11157–11165.

97 M. Yan, Y. Yao, J. Wen, L. Long, M. Kong, G. Zhang, X. Liao, G. Yin and Z. Huang, Construction of a Hierarchical $NiCo_2S_4$@PPy Core–Shell Heterostructure Nanotube Array on Ni Foam for a High-Performance Asymmetric Supercapacitor, *ACS Appl. Mater. Interfaces*, 2016, **8**, 24525–24535.